GENETICS

Integrated -omics approach reveals persistent DNA damage rewires lipid metabolism and histone hyperacetylation via MYS-1/Tip60

Shruthi Hamsanathan[1], Tamil Anthonymuthu[2,3,4], Suhao Han[1], Himaly Shinglot[1], Ella Siefken[1], Austin Sims[1], Payel Sen[5], Hannah L. Pepper[6], Nathaniel W. Snyder[6], Hulya Bayir[2,3,7], Valerian Kagan[3,7], Aditi U. Gurkar[1,8,9]*

Although DNA damage is intricately linked to metabolism, the metabolic alterations that occur in response to DNA damage are not well understood. We use a DNA repair–deficient model of ERCC1-XPF in *Caenorhabditis elegans* to gain insights on how genotoxic stress drives aging. Using multi-omic approach, we discover that nuclear DNA damage promotes mitochondrial β-oxidation and drives a global loss of fat depots. This metabolic shift to β-oxidation generates acetyl–coenzyme A to promote histone hyperacetylation and an associated change in expression of immune-effector and cytochrome genes. We identify the histone acetyltransferase MYS-1, as a critical regulator of this metabolic-epigenetic axis. We show that in response to DNA damage, polyunsaturated fatty acids, especially arachidonic acid (AA) and AA-related lipid mediators, are elevated and this is dependent on *mys-1*. Together, these findings reveal that DNA damage alters the metabolic-epigenetic axis to drive an immune-like response that can promote age-associated decline.

INTRODUCTION

Persistent DNA damage not only promotes developmental disorders but also drives a range of age-related chronic conditions like metabolic syndrome, cardiovascular disease, cancer, and neurodegeneration (*1*). Technological advances have strengthened the evidence for accumulation of DNA damaging lesions and DNA mutations with age and disease in several model organisms, as well as humans (*2*–*5*). In humans, several inborn mutations of genes linked to DNA repair are associated with progeroid syndromes (*2*). Furthermore, pediatric cancer patients treated with DNA damaging chemotherapeutic drugs or radiotherapy have increased survival rates but often exhibit frailty and develop multiorgan aging pathologies in their mid-40s (*6*–*8*). Given that DNA damage occurs continuously throughout life, discerning the underlying mechanism of how genotoxic stress contributes to health and disease is critical.

Nuclear DNA repair is intimately tied to metabolism. In response to acute nuclear genotoxic stress, metabolic pathways regulate the availability of metabolite pools, which are essential for the DNA repair process (*9*, *10*). In contrast, the full range of metabolic alterations that occur in response to persistent DNA damage are not well understood. Certain interventions that target the metabolic node can alleviate persistent DNA damage–driven age-associated pathologies. For example, in *Ercc1*$^{-/\Delta}$ mice, a model where persistent DNA damage occurs because of loss of a DNA repair endonuclease, dietary restriction substantially improved healthspan and extended lifespan (*11*). In *Csb*$^{-/-}$ mice and in *Caenorhabditis elegans* rendered deficient in transcription-coupled nucleotide excision repair (TC-NER), a model of Cockayne syndrome, supplementation with a nicotinamide adenine dinucleotide (NAD^+) precursor reversed metabolic, mitochondrial, and transcriptional changes, and improved overall health (*12*, *13*).

Recent evidence has uncovered cellular metabolism as a modifier of the epigenome, providing support for the metabolic-epigenetic axis. For example, β-oxidation is the multistep mitochondrial process of breaking down long chain fatty acid (LCFA) into units of acetyl–coenzyme A (CoA). Acetyl-CoA is critical for histone acetylation and gene expression (*14*). Some studies have reported changes to the epigenome in response to acute genotoxic stress (*9*). Similarly, there is evidence that suggests that DNA damage may reprogram aspects of cellular metabolism (*15*–*17*). However, whether the metabolic-epigenetic axis is altered in response to persistent DNA damage and whether these changes have an impact on organismal health are currently unknown.

ERCC1 (excision repair cross complementing-group 1) is a DNA repair protein that forms a heterodimer with XPF (xeroderma pigmentosum group F-complementing protein) and functions as a 5′-3′ structure-specific endonuclease. XPF contains the catalytic domain, whereas ERCC1 stabilizes the DNA repair complex, such that loss of ERCC1 leads to loss of XPF activity. ERCC1-XPF is required for multiple nuclear DNA repair mechanisms that include NER, DNA interstrand cross-link repair, and double-strand break repair (*18*). Because ERCC1-XPF is involved in multiple DNA repair pathways, patients lacking this complex exhibit phenotypically pleiotropic syndromes including XFE syndrome, Cockayne syndrome, and cerebro-oculo-facial skeletal syndrome or cancer-prone disorders such as xeroderma pigmentosum (*2*). Like XFE progeroid patients, loss of ERCC1-XPF in mouse models spontaneously leads to an accelerated aging phenotype that includes progressive sarcopenia,

[1]Aging Institute of UPMC and the University of Pittsburgh School of Medicine, 100 Technology Dr., Pittsburgh, PA 15219, USA. [2]Department of Critical Care Medicine, University of Pittsburgh School of Medicine, Pittsburgh, PA 15260, USA. [3]Children's Neuroscience Institute, Children's Hospital of Pittsburgh, University of Pittsburgh, Pittsburgh, PA 15224, USA. [4]Adeptrix Corp., Beverly, MA 01915, USA. [5]Laboratory of Genetics and Genomics, National Institute on Aging, National Institutes of Health, Baltimore, MD 21224, USA. [6]Center for Metabolic Disease Research, Department of Cardiovascular Sciences, Lewis Katz School of Medicine at Temple University, Philadelphia, PA 19140, USA. [7]Department of Environmental Occupational Health, Graduate School of Public Health, University of Pittsburgh, Pittsburgh, PA 15260, USA. [8]Division of Geriatric Medicine, Department of Medicine, University of Pittsburgh School of Medicine, 3471 Fifth Avenue, Kaufmann Medical Building Suite 500, Pittsburgh, PA 15213, USA. [9]Geriatric Research, Education and Clinical Center, Veterans Affairs Pittsburgh Healthcare System, Pittsburgh, PA 15240, USA.
*Corresponding author. Email: agurkar1@pitt.edu

osteoporosis, cardiovascular disease, neurodegeneration, and other well-known age-related morbidities (*19*). To examine the complex effect of physiologically relevant, persistent endogenous DNA damage on health, we used *C. elegans* as a model system. Phenotypes associated with loss of ERCC1-XPF in mammals is recapitulated in *C. elegans*, including increased susceptibility to DNA damaging agents, accumulation of endogenous DNA lesions, and premature aging (*20*, *21*).

We have previously demonstrated that it is not the DNA damage per se that drives the onset of disease but rather the DNA damage–induced cellular responses that ultimately promote a decline in health (*20*). In particular, there is an initial genotoxic stress-"adaptive" response, during which ERCC1-XPF–deficient *C. elegans* and mice do not display any functional decline and are resistant to a number of stressors (*20*, *22*). However, with persistent DNA damage, there is an "exhaustion" of this response leading to augmented stress sensitivity and physiological deterioration (*20*, *21*). A large gap in our knowledge is the mechanistic understanding of the cellular and molecular alterations that happen during this exhaustive phase. The identification of these molecular alterations is critical for the rational development of strategies to promote health and homeostasis.

RESULTS

Persistent DNA damage reprograms lipid metabolism

To gain a comprehensive understanding of the cellular and metabolic responses to genotoxic stress during the "exhaustive" phase, we performed an integrated multi-omic analysis, combining transcriptomics and metabolomics. We analyzed global changes in the transcriptome of *xpf-1* worms in midlife [day 7 (D7) of adulthood], when they start displaying increased stress sensitivity but before any evidence of increased mortality (*20*, *21*). In total, 8827 differential expressed genes ($q < 0.05$) were identified in *xpf-1* mutants compared to wild-type (N2); 4521 up-regulated genes and 4306 down-regulated genes (Fig. 1A). Enrichment analysis of differentially expressed genes using WormCat tool (*23*) showed an up-regulation of genes particularly involved in metabolism, stress response, signaling, and mRNA functions (Fig. 1B).

Molecular changes in response to stimulants such as DNA damage can affect both at the transcriptomic and metabolomic levels. Therefore, we also analyzed the metabolome of N2 and *xpf-1* worms at D7. Our global metabolomic analysis using high-resolution liquid chromatography mass spectrometry (HR-LC-MS) identified 4229 features. We noted that 853 metabolic features were elevated in N2 worms while 1521 were elevated in the *xpf-1* worms (Fig. 1C). Multivariate analysis using principal components analysis (PCA) revealed a significant difference between the metabolome of N2 and *xpf-1* worms (Fig. 1D). To capture the changes in biological processes ensuing with persistent DNA damage at a systemic level, we performed a multi-omic data integration of transcriptomics and metabolomics data. Using Multiomics Factor Analysis (MOFA) framework, we first identified transcripts and metabolic features that showed a coordinated increase in *xpf-1* compared to N2 (*24*). Enrichment analysis of highly coordinated sets showed that metabolism, specifically lipid metabolism, was significantly up-regulated in *xpf-1* mutants ($P < 0.05$; Fig. 1, E and F). Other pathways identified through enrichment analysis such as cell cycle, mRNA functions, and proteolysis were insignificant ($P > 0.05$). Together, our multi-omic analysis suggests that persistent DNA damage rewires metabolism particularly toward lipid metabolism.

Since lipid metabolism was significantly altered in *xpf-1* mutants, we examined temporal changes in fat depots using Oil-red-O (ORO). ORO staining is a semiquantitative method that is used to measure lipid changes in *C. elegans* and it primarily stains neutral lipids such as triacylglycerides (TAG) (*25*). At D7, *xpf*-1 and *ercc-1* mutants exhibited significantly decreased ORO staining compared to N2 (Fig. 1, G and H). Consistent with these results, biochemical quantitation of total TAG levels in *xpf-1* worms showed a substantial decrease (Fig. 1I). No changes in the levels of phospholipid (PL) content were observed in these animals (Fig. 1J). To determine whether the loss of fat stores was a feature of the exhaustive phase in response to persistent DNA damage, we analyzed *xpf-1* and *ercc-1* worms as young adults [day 2 (D2) of adulthood-adaptive phase-stress resistant]. At D2, ORO staining in *xpf-1* worms was not significantly affected. Consistent with this, we did not observe any changes in TAG and PL levels in young *xpf-1* adults (fig. S1, A to C). These findings indicated that lipid stores in DNA repair mutant worms decline rapidly by midlife. Although the loss of fat depots was evident at D7, the decrease in ORO staining was noticeable in *xpf-1* animals by D5 (fig. S1D). To rule out the possibility of germline signaling in the regulation of fat depots, we examined ORO staining in *glp-4* mutants, which are defective in germline proliferation (*25*). Consistent with *ercc-1* mutants, *ercc-1 glp-4* double mutants showed reduced ORO staining compared to *glp-4* animals, indicating that the loss of fat depots in DNA repair mutants is not influenced by germline proliferation/germline stem cell signaling (fig. S1E). These results suggest that persistent DNA damage results in significant loss of fat stores.

Lipolysis is augmented upon persistent DNA damage

The exhaustion of lipid stores in DNA repair mutants can be attributed to either defects in lipid synthesis or an increase in lipid catabolic processes. We first examined lipid synthesis genes by reverse transcriptase quantitative polymerase chain reaction (RT-qPCR). Fatty acid synthase (FASN-1) encodes a multienzyme complex with six catalytic activities including fatty acid synthase activity, whereas *pod-2* catalyzes the rate-limiting step of generating malonyl-CoA from acetyl-CoA, which is then used by FASN-1 to synthesize fatty acids (*26*). Both *fasn-1* and *pod-2* were not significantly affected in *xpf-1* mutants (Fig. 2A and fig. S2A). Previous reports indicate that expression of fatty acid desaturases correlate with the fat levels in the *C. elegans* (*27*). qPCR analysis of the seven desaturases (*fat1* to *fat7)* showed increase expression of *fat-1*, *fat-4*, and *fat-7* in *xpf-1* animals (fig. S2B). These results suggest that the loss of fat depots observed is likely not due to impaired lipid synthesis but rather an increase in lipid catabolic processes. Most of the lipid metabolic processes in *C. elegans* occur in the intestine where the animals store fat as droplet structures mainly composed of TAG. During lipid catabolism, first, the lipid droplets are hydrolyzed by intestinal lysosomal lipases that breakdown TAGs to free fatty acids (Fig. 2B). RT-qPCR analysis showed increased mRNA expression of two lipases, *lipl-1* and *lipl-3*, but no changes in *lipl-4* in *xpf-1* mutants (Fig. 2C). Knockdown by RNA interference (RNAi) starting at day 1 of adulthood of both *lipl-1* and *lipl-3* restored fat depots in *xpf-1* mutants to that of N2, suggesting that the loss of fat stores observed in *xpf-1* is a result of augmented lipolysis (Fig. 2D).

Next, to examine the lipid profile changes in response to persistent DNA damage, we performed an in-depth lipidomic analysis. *C. elegans*, like mammals, have TAGs that contain mono-unsaturated

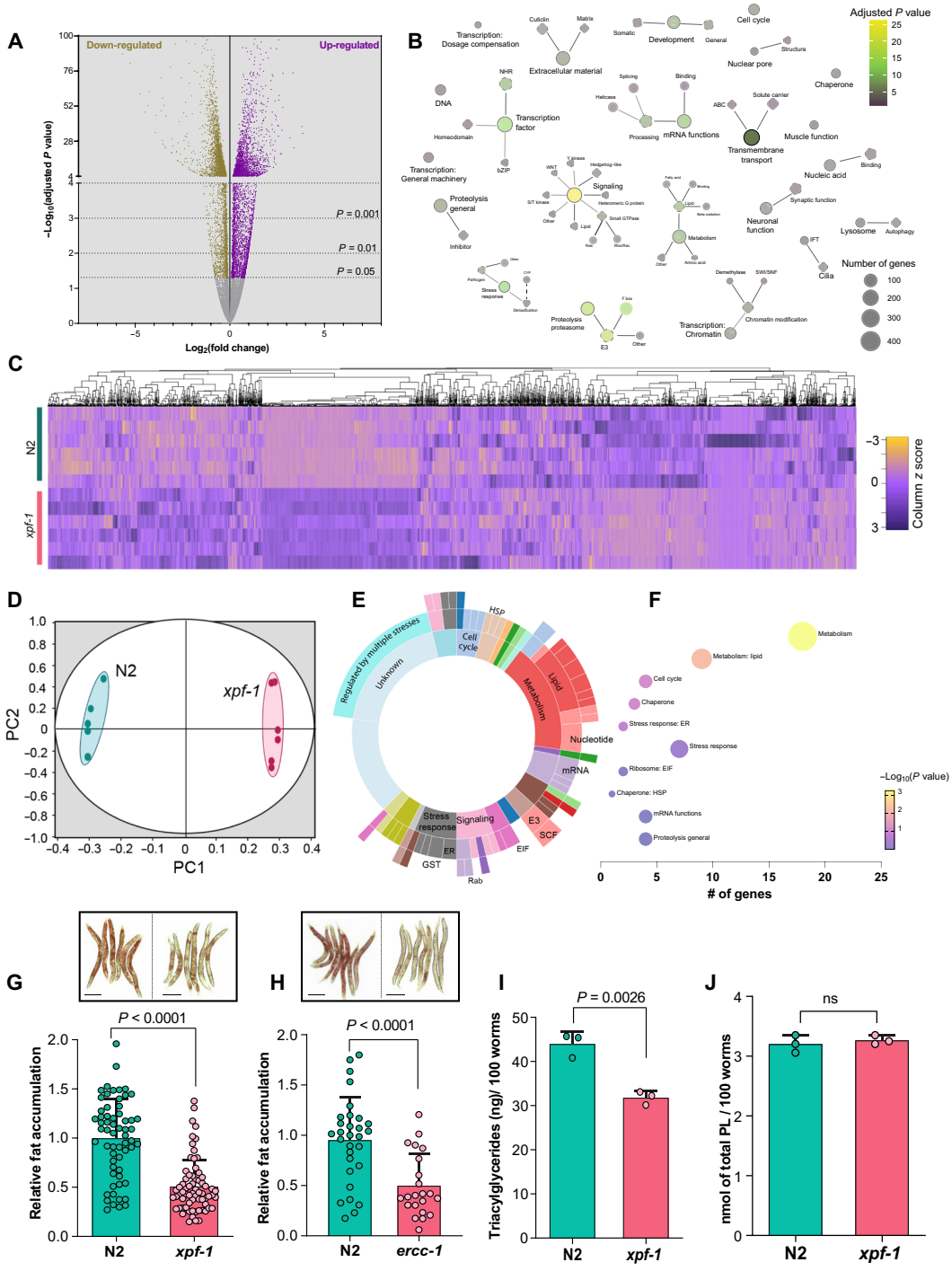

Fig. 1. Persistent DNA damage rewires lipid metabolism. (**A**) Volcano plot of differentially expressed genes in *xpf-1* at day 7 (D7) adulthood. Horizontal gray lines denote adjusted *P* value cutoffs of 0.05, 0.01, and 0.001. The number of genes that are up-regulated (purple) or down-regulated (gold) significantly ($P < 0.05$) is indicated. $n = 6$ biological replicates. (**B**) Network diagram showing statistically significant pathways represented by up-regulated genes (adjusted $P > 0.05$) in *xpf-1* at D7. Nodes with solid border line: pathway category 1; nodes with dashed border line: category 2; nodes without borderline: category 3, as defined in WormCat. (**C**) Heatmap showing changes in abundance of metabolites identified from the metabolomics analysis in N2 and *xpf-1*. (**D**) Dot plot representing the principal components analysis (PCA) of metabolites identified from the metabolomics analysis in N2 and *xpf-1*. $n = 6$ biological replicates. (**E**) Sunburst plot showing significantly enriched categories obtained from genes that showed coordinated increase with metabolomics data, analyzed using Multi-Omics Factor Analysis V2. (**F**) Bubble plot showing enriched pathways represented by the highly correlated transcriptome and metabolome. ER, Endoplasmic Reticulum; EIF, Eukaryotic Initiation Factors; SCF, Skp; Cullin, F-box containing complex; GST, Glutathione S-transferases; HSP, Heat Shock proteins. (**G** and **H**) Distribution of relative fat depots as measured by Oil-red-O (ORO) staining in (G) N2 and *xpf-1* worms. $n \geq 61$ (H) N2 and *ercc-1*. $n \geq 22$ (H). Data are means ± SD. Inset shows representative ORO-stained images. Scale bars, 200 μM. Two tailed, Student's *t* test. (**I**) Total triglycerides (TAG) (**J**) and total phospholipid (PL) levels in N2 and *xpf-1*. Data are means ± SD. Two-tailed Student's *t* test, $n = 3$ biological replicates. All experiments were performed with D7 worms. ns, not significant.

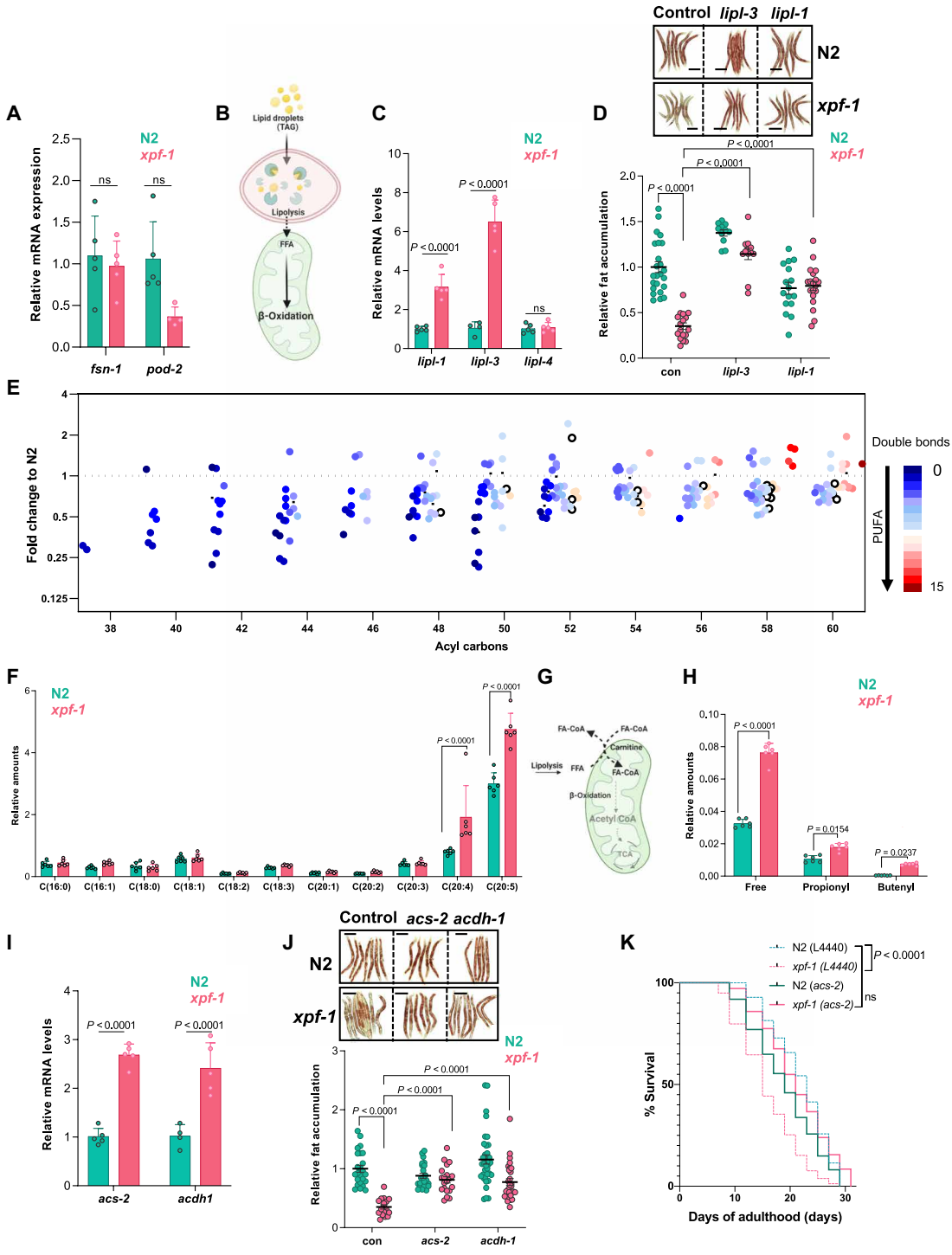

Fig. 2. Increased lipolysis and mitochondrial β-oxidation in response to persistent DNA damage. (**A**) mRNA levels (from qPCR) of fatty acid synthesis genes in N2 and *xpf-1*. $n = 5$ biological replicates. Two-way analysis of variance (ANOVA), Sidak correction. (**B**) TAG lipid droplets broken down by lipases in lysosomes to release free fatty acids that enter mitochondria for β-oxidation. (**C**) mRNA levels (from qPCR) of lysosomal lipases in N2 and *xpf-1* animals. $n = 5$. (**D**) Fat stores in N2 and *xpf-1* animals fed RNAi against control (L4440), *lipl-3* and *lipl-1*. $n > 11$ worms per condition, two independent experiments. Two-way ANOVA, Tukey's test. Scale bars, 200 μM. (**E**) Fold change of TAG lipids (from lipidomics) in *xpf-1* compared to N2. Abscissa represents the total acyl carbons in the TAG molecules, and color represents the number of double bonds. Only significantly changed lipids are shown here (two-tailed Student's *t* test $P < 0.05$). (**F**) Relative amounts of free fatty acids from lipidomics analysis $n = 6$. Two-way ANOVA, Sidak correction. (**G**) Free fatty acid mobilization into mitochondria for β-oxidation. (**H**) Levels of free and short-chain carnitines in N2 and *xpf-1*. $n = 6$. Two-way ANOVA, Sidak correction. (**I**) mRNA levels (from qPCR) of β-oxidation genes in N2 and *xpf-1* mutant animals. $n = 6$. (**J**) ORO-stained images (top) and relative fat levels (bottom) in N2 and *xpf-1* fed with RNAi against L4440, *acs-2* and *acdh-1*. $n > 17$ worms per condition, two independent experiments, two-way ANOVA, Tukey's test. Scale bars, 200 μM. (**K**) Survival of N2 and *xpf-1* grown on L4440 or *acs-2* RNAi from day 1 of adulthood. Log-rank (Mantel-Cox) test. All data are means ± SD from day 7 worms.

fatty acids (MUFAs), polyunsaturated fatty acids (PUFAs), and saturated fatty acids (SFAs). Consistent with an increase in lipolysis, we observed ~58% of TAG species were significantly reduced in *xpf-1* animals (Fig. 2E). Primarily, highly abundant isobaric species of TG 52:2, TG 50:2, TG 54:3, TG 50:3, TG 48:2, TG 50:1, TG 48:1, and TG 52:3 were reduced, suggesting hydrolysis of mostly MUFA containing TAGs. TAGs (~13%) were significantly elevated in *xpf-1* mutants compared to N2. Among the increased TAGs, 78% had at least one PUFA (double bond >3) suggesting a selective synthesis/regeneration of PUFA containing TAGs. Furthermore, lipidomic profiling of free fatty acids in *xpf-1* animals revealed that SFAs, such as palmitic acid (16:0), steric acid (18:0), arachidic acid (20:0), and MUFAs such as palmitoleic acid (16:1), oleic acid (18:1), and eicosenoic acid (20:1), were unchanged (Fig. 2F). Major long chain SFAs and MUFAs (≤18 carbon) usually enter mitochondria for fatty acid oxidation, implying that these free fatty acids may be used for the subsequent β-oxidation step (Fig. 2G). In contrast, two major PUFAs, arachidonic acid (AA; 20:4) and eicosapentaenoic acid (EPA; 20:5), were elevated in *xpf-1* mutants, whereas minor PUFAs including linoleic acid (18:2), eicosadienoic acid (20:2), and dihomo-γ-linolenic acid (20:3) were unaltered (Fig. 2F). Together, these results indicate an increase in breakdown of lipid depots and enrichment of free PUFAs in response to persistent DNA damage.

Increased fatty acid oxidation (β-oxidation) in DNA repair–deficient mutants

Upon lipolysis, LCFA may enter the mitochondria for β-oxidation. However, the mitochondrial membrane is impermeable to LCFA. Hence, LCFA must be conjugated to carnitine to enter the mitochondria. Metabolomic data showed an increase in free and short-chain acylcarnitine levels (putative identification of butyl- and propenylcarnitine) in *xpf-1* mutants suggesting an up-regulation in β-oxidation (Fig. 2H and fig. S2D). Consistent with this metabolomics data, transcriptional levels of genes regulating mitochondrial β-oxidation genes, including *acs-2* and *acdh-1*, were significantly increased in *xpf-1* mutants (Fig. 2I and fig. S2E). ACS-2 encodes an acyl-CoA synthetase that activates fatty acids for transport into the mitochondria (*28*), whereas ACDH-1 encodes a mitochondrial short-chain acyl-CoA dehydrogenase (*29*) that catalyzes the initial enzymatic reaction of β-oxidation. RNAi-mediated knockdown of both *acs-2* and *acdh-1* in *xpf-1* adults rescued the loss-of-fat phenotype (Fig. 2J). These results were recapitulated in *ercc-1* mutants following *acs-2* knockdown as well (fig. S3A), suggesting that the fat stores are depleted in DNA repair mutants as a consequence of increased β-oxidation.

We next performed a RNAi screen for potential transcription factors that could be regulating lipid metabolism in *xpf-1* mutants, using RNAi reported in previous studies (*30*, *31*). None of the tested transcriptional regulators involved in lipid metabolism, including *hlh-30* [mammalian homolog TFEB(Transcription Factor EB)], *nhr-49* (thought to function similarly to peroxisome proliferator–activated receptor α), *nhr-80* [thought to function similarly to Hepatocyte Nuclear Factor 4 (HNF4)], *sbp-1* (Sterol regulatory-element binding proteins, SREBP), and *mdt-15* [Mediator Complex Subunit 15 (MED15)] rescued the DNA damage–induced loss of fat depots (fig. S3B). Overall, these results indicate that persistent DNA damage drives a metabolic switch to β-oxidation, most likely independent of the canonical lipid metabolic transcription factors. We then examined whether the induction of mitochondrial β-oxidation in DNA repair–deficient mutants is associated with their shortened lifespan. RNAi knockdown of *acs-2* not only restored fat accumulation but also rescued the shortened lifespan in *xpf-1* animals (Fig. 2K). Together, these data suggest that there is an increase in β-oxidation in *xpf-1* mutants, and inhibiting mitochondrial β-oxidation restores lifespan.

Persistent DNA damage increases β-oxidation for generation of acetyl-CoA

β-Oxidation breaks down fatty acids to generate acetyl-CoA, a metabolite that not only plays a pivotal role in energy production and macromolecular synthesis but also acts as a sole donor for acetylation (*14*). Acetyl-CoA can have multiple fates including entering the tricarboxylic acid (TCA) cycle to ultimately generate adenosine triphosphate (ATP). Metabolomic profiling of TCA metabolites showed that the levels of citrate, fumarate, and malate were not significantly affected in *xpf-1* mutants (Fig. 3A). Consistent with these results, the mRNA levels of genes involved in the production of these metabolites were not affected (Fig. 3B). Key glycolytic metabolites such as hexose, hexose-6-phosphate, and pyruvate, which link to acetyl-CoA production and the TCA cycle, were also not altered (Fig. 3A). Furthermore, amino acid levels were not changed between N2 and *xpf-1* animals, except for valine and glutamine (fig. S4A). Both valine and glutamine can feed into TCA cycle to increase the levels of succinate. Succinate, a key metabolite that connects TCA cycle to electron transport chain, was elevated in *xpf-1* mutants (Fig. 3A) and was paralleled with no change in succinate dehydrogenase B and D enzymes (Fig. 3B). It must be noted that the levels of metabolites downstream of succinate, such as malate and fumarate, were unaltered in *xpf-1* mutants, suggesting that the increase in valine and glutamine has little effect on the overall output of the TCA cycle. These data suggest that the steady-state TCA cycle is not altered markedly upon persistent DNA damage.

Next, we wanted to directly test whether the increase in β-oxidation leading to loss of fat stores in *xpf-1* mutants was primarily for the generation of acetyl-CoA. We reasoned that if *xpf-1* mutants were up-regulating β-oxidation to generate acetyl-CoA, then supplementation with metabolites known to directly produce acetyl-CoA would rescue β-oxidation and thus subsequent loss of fat stores. We supplemented the N2 and *xpf-1* nematodes with three metabolites known to directly produce acetyl-CoA: citrate, pyruvate, and acetate (Fig. 3C). Citrate that can be converted into acetyl-CoA either by ATP-citrate lyase (*acly*/ACLY) or through the TCA cycle did not rescue the fat stores in *xpf-1* mutant, suggesting that both these routes are unable to generate acetyl-CoA (Fig. 3, D and E). Pyruvate and acetate are converted to acetyl-CoA by pyruvate dehydrogenase (*pdh*/PDH) and acyl-CoA synthetase (*acs-19*/ACSS2), respectively. Supplementation with either pyruvate or acetate rescued the loss of fat stores in *xpf-1* and *ercc-1* mutants (Fig. 3, D, F, and G, and fig. S4B). We did not observe a substantial difference in the total acetyl-CoA concentration between *xpf-1* and N2 worms (fig. S4, C and D). However, we observed an increase in acetyl-CoA–dependent metabolites. A number of acetylated amino acids and amino acid derivatives were increased in *xpf-1* worms (fig. S4, E to N). Furthermore, we observed an increase in acetoacetate (putative identification) in *xpf-1* worms through metabolomic fragmentation analysis (Fig. 3H), which is a product of mitochondrial compartmentalized acetyl-CoA via ketogenesis. Similarly, we observed an increase in acetyl-carnitine levels in the *xpf-1* mutants, suggesting the potential export of acetyl-CoA from the mitochondria (Fig. 3I). Together,

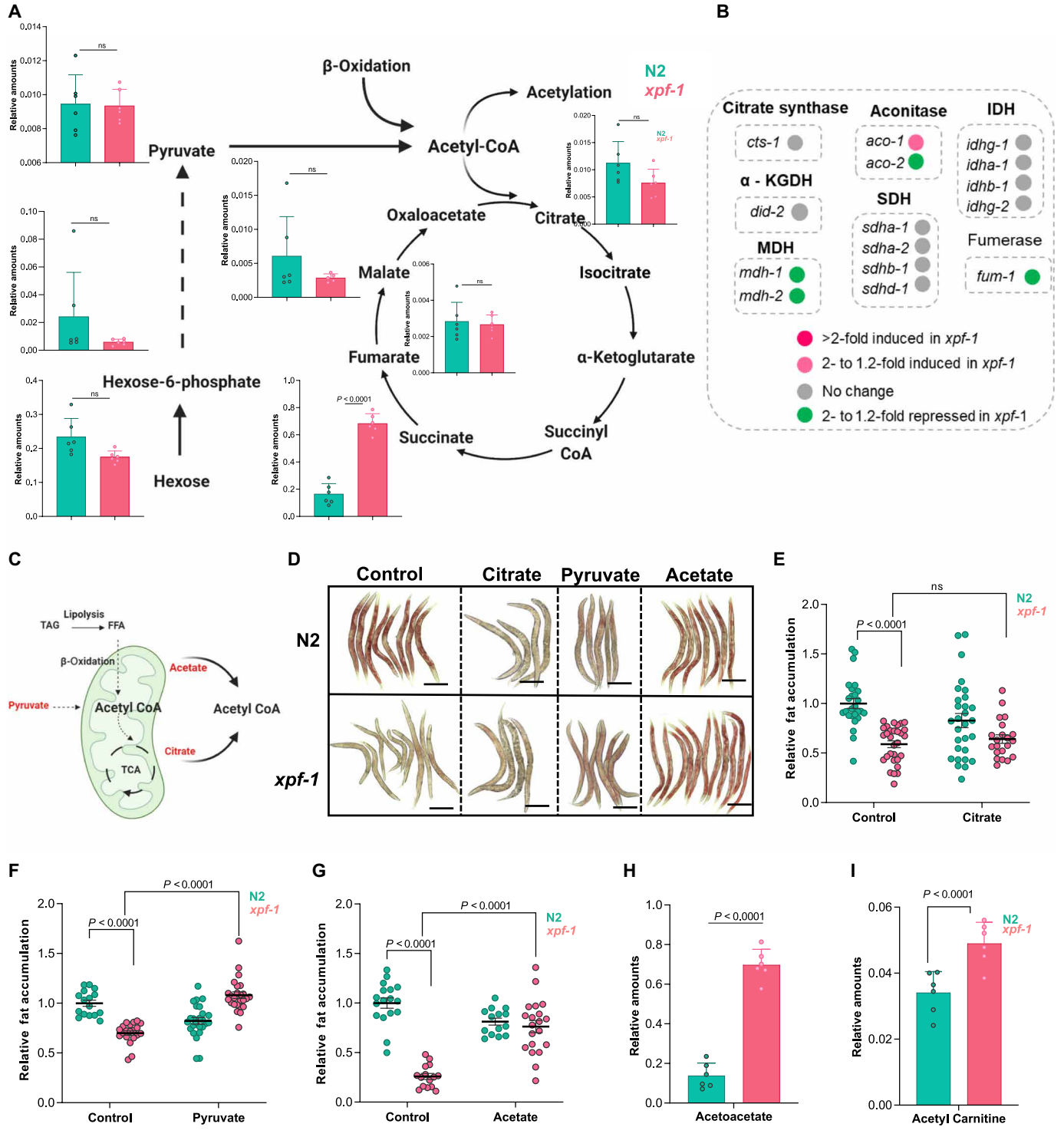

Fig. 3. Increased β-oxidation in *xpf-1* is used to generate acetyl-CoA. (**A**) Glycolysis and TCA cycle metabolite levels in N2 and *xpf-1*. $n = 6$ biologically independent experiments, Student's two-tailed *t* test. (**B**) TCA metabolic gene expression profiles (from RNA sequencing) between N2 and *xpf-1*. (**C**) Schema illustrating sources of acetyl-CoA production. Metabolites in red when supplemented exogenously can generate acetyl-CoA. (**D**) Representative ORO-stained images. Scale bars, 200 μM and (**E** to **G**) quantitation of fat stores in N2 and *xpf-1* in control or supplemented with (E) citrate, (F) pyruvate, and (G) acetate. $n > 14$ worms per condition, two to four independent experiments. Data are means ± SD two-way ANOVA, Tukey's test. (**H**) Levels of acetoacetate, a product of acetyl-CoA in N2 and *xpf-1*. Data are derived from metabolomics analysis. $n = 6$ biologically independent experiments, Student's two-tailed *t* test. (**I**) Relative amount of acetyl carnitines in N2 and *xpf-1* worms. Data from metabolomics analysis. $n = 6$ biologically independent experiments. Data are means ± SD Student's *t* test. All experiments were performed with D7 worms.

our findings suggest that DNA repair mutants drive mitochondrial β-oxidation to generate acetyl-CoA.

β-Oxidation–derived acetyl-CoA promotes histone hyperacetylation

Acetyl-CoA is a sole donor of acetyl groups for histone and non-histone acetylation (Fig. 4A) (*32*). Previously, it was reported that mitochondrial β-oxidation is the predominant contributor for histone acetylation, chromatin regulation, and gene transcription (*33*). Acetyl-CoA is impermeant to the inner mitochondrial membrane and needs to be transported into or generated locally in the nucleus for histone acetylation (*34*). Acetyl-carnitines are known to shuttle acetyl-CoA from mitochondria into the nucleus and are significantly elevated in *xpf-1* mutants (Fig. 3I) (*35*). Therefore, we next examined key histone acetylation marks associated with DNA damage, as well as aging, histone H3K, and histone H4K. Histone 4 lysine 16 acetylation (H4K16ac) opens chromatin by reducing the internucleosomal interactions (*36*). On the other hand, histone 3 lysine 9 acetylation (H3K9) acetylation is elevated in the region surrounding the transcription start sites of active genes indicating its role in transcriptional initiation (Fig. 4A). To probe multiple histone acetylation marks, we used bead-assisted mass spectrometry (BAMS) approach (*37*). In this method, protease-digested histone peptides were isolated using antigen-bound immuno-affinity beads and analyzed through mass spectrometry. This approach allows for the detection of histones that have undergone several posttranslational modifications including acetylation. We used two types of beads coated with H3K9ac and H4K5K8K12K16ac antibodies to capture acetylated histone from histone H3 and histone H4, respectively. Four histone H4 peptides and 10 histone H3 peptides were identified during this analysis (table S4). Histone H3 segments have one to three acetylations, while histone H4 fragments have three to four acetylations (Fig. 4, B and C). The multi-acetylated histone H4 fragments were found to be higher in *xpf-1* compared to N2 ($P = 0.028$) animals. In *xpf-1* mutants, two peptide species were significantly elevated: ac-^{2}SGRG KacGGKacGLGKacGGAK^{16} ([2-20] +3 ac) and ac-^{2}SGRGKacGGKacGLGKacGGAKacRHRK^{20} ([1-20] +4 ac; Fig. 4, B and C) suggesting hyper-acetylation of H4K9, H4K12, and H4K16 in *xpf-1* worms. The one and two acetylated peptides in histone H3 were similar in N2 and *xpf-1* mutants (fig. S5A). However, the *xpf-1* mutants have considerably higher levels of three acetylated peptides ($P = 0.018$), with ^{5}QTARKacSTGGKacAPRKacQLATK^{23} ([5-23] +3 ac) being the significantly increased species, suggesting hyperacetylation of H3K9, H3K14, and H3K18 (Fig. 4, B and C). These results clearly demonstrate a hyper-histone acetylation state in the *xpf-1* mutant. H4K16ac and H3K9ac marks were significantly increased in *xpf-1* mutants compared to N2 by Western blot, as well (Fig. 4D and fig. S5, C and D).

Previously, it was shown that variations in H4 acetylation levels positively correlated with nuclear size (*38*). Since we observed histone hyperacetylation, which leads to open chromatin conformation, we examined the nuclear size in intestinal cells of *xpf-1* nematodes. DAPI (4′,6-diamidino-2-phenylindole)–stained intestinal nuclei in *xpf-1* mutants were enlarged by ~40% (N2:169.3 ± 8.0 μm^2; *xpf-1*: 237.6 ± 9.8 μm^2), thus indicating a "loose" chromatin structure (Fig. 4E). Knockdown of *acs-2* in these animals reduced H4K16 hyperacetylation and restored nuclear size toward N2 (189.1 ± 10 μm^2; Fig. 4, F to H). These findings suggest that the up-regulated β-oxidation in *xpf-1* mutants is associated with hyperacetylation of histones affecting global changes in chromatin structure. Open chromatin structure and histone (H3K9 and H4K16) acetylation are also typically associated with enhanced gene expression. Consistent with this, our RNA sequencing (RNA-seq) data showed an increase in global gene expression levels (Fig. 1A). Specifically, an up-regulation of "immune-like signature genes" involved in innate immunity and stress response, including C-type lectins (*clecs*) and cytochrome P450s (*cyp*) genes, was observed in *xpf-1* worms (fig. S6, A and B). CYPs in particular are stress response genes that belong to a family of diverse monooxygenases, which oxidize fatty acids, sterols, and endogenous compounds. Up-regulated CYP expression in *xpf-1* mutants was substantiated with RT-qPCR data (Fig. 4I). Thus, persistent DNA damage promotes histone hyperacetylation and up-regulation of an immune-effector gene transcription program.

MYS-1 controls histone hyperacetylation in response to persistent DNA damage

Histone acetylation is a highly regulated process governed by two enzyme groups, histone acetyl transferases (HATs) and histone deacetylases (HDACs). HATs transfer acetyl groups from acetyl-CoA to an ε-amino group of a histone lysine residues. On the other hand, HDACs remove acetyl groups from acetylated histones. Balance between HATs and HDACs plays a crucial role to regulate chromatin dynamics and gene expression and to maintain homeostasis (Fig. 5A). To determine the HATs involved in histone hyperacetylation in *xpf-1* mutants, we performed an RNAi screen targeting putative HATs. We reasoned that since acetyl-CoA is an obligatory cofactor of HATs, knockdown of the involved HAT would avert the increased demand for acetyl-CoA. This would thus relieve the need for augmented β-oxidation and rescue the loss of fat stores in *xpf-1* nematodes. We knocked down three subfamilies of HAT-1 class previously known to play a role in DNA damage recognition and repair: *pcaf-1* [mammalian homolog P300/CBP-associated factor (PCAF)], *mys-1* (Tip60), and *cbp-1* [CREB binding protein (CBP)/p300)] (*39*). Only *mys-1* knockdown resulted in the rescue of fat stores in *xpf-1* mutants suggesting its role in acetylation, using β-oxidation–derived acetyl-CoA (Fig. 5B). Fat reserves were similarly rescued in *ercc-1* mutants after *mys-1* knockdown. (fig. 3A). BAMS assay also demonstrated a significant reduction in overall hyperacetylation of H4 and H3 upon *mys-1* knockdown in *xpf-1* mutants (Fig. 5C and fig. S5B). Consistent with these findings, the level of H4K16ac was also reduced upon *mys-1* knockdown (Fig. 5D and fig. 5D). We next examined whether the increased nuclear size in *xpf-1* mutants was also rescued upon suppression of *mys-1*. DAPI staining of intestinal nuclei in *xpf-1* (*mys-1* RNAi) exhibited compact nuclei (Fig. 5, E and F). Since *mys-1* knockdown restored fat depots and decreased histone hyperacetylation and nuclear size, we next examined its effects on lifespan of *xpf-1* mutants. Suppression of *mys-1* rescued the shortened lifespan of *xpf-1* and *ercc-1* worms (Fig. 5G and fig. S3C). Next, we assessed the HDACs involved in the DNA damage–driven metabolic-epigenetic axis. Since HDACs deacetylate histones, inhibition of involved HDAC would prevent additional demand for acetyl-CoA and therefore rescue fat stores. A targeted RNAi screen for HDACs *hda-1*, *hda-3*, and *sir-2.1* revealed that only *sir-2.1* led to increased fat stores in *xpf-1* mutants (Fig. 5H). We also tested the effect of *sir2.1* knockdown in *ercc-1* mutant, which showed similar results to that of *xpf-1* mutants (fig. S3A). As expected, *sir-2.1* knockdown did not affect the intestinal nuclei size in *xpf-1* animals (Fig. 5, I and J). Likewise, *sir-2.1* knockdown did not alter the shortened

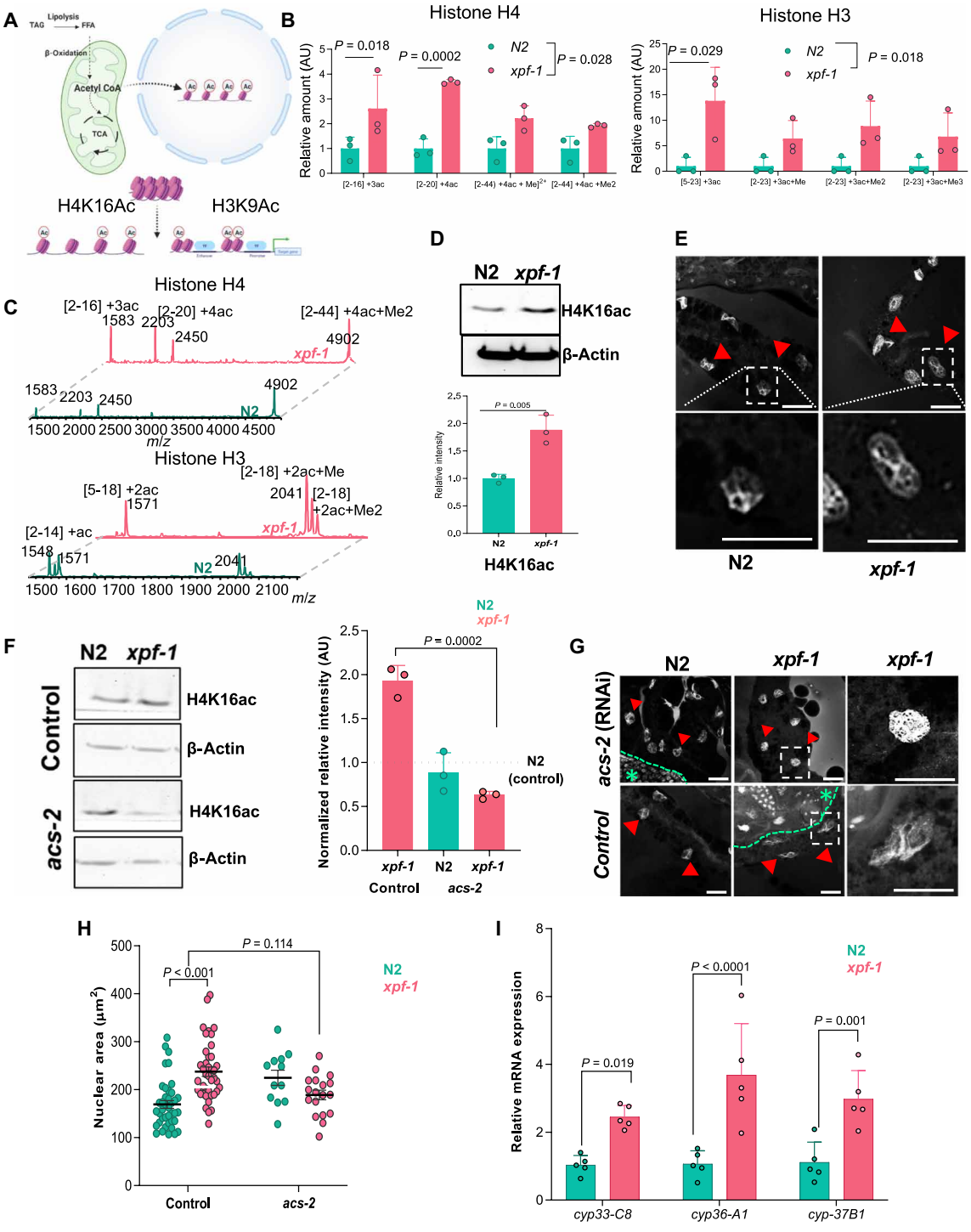

Fig. 4. Increased β-oxidation drives histone acetylation upon persistent DNA damage. (**A**) Illustration showing increased β-oxidation leads to an increase in acetyl-CoA pools that is used for histone acetylation such as H4K16ac in the nucleus. (**B**) Relative levels of hyperacetylated histone H4 (left) and H3 (right) peptides measured using BAMS assay. $n = 3$, two-way ANOVA, Sidak correction. (**C**) Representative mass spectrum (top) histone H4 (bottom) and H3 peptides from BAMS assay. (**D**) Immunoblots (top) of histone H4K16ac and its quantitation relative to β-actin (bottom) in N2 and *xpf-1*. $n = 3$. Data are means ± SD ,two-tailed Student's *t* test. (**E**) Representative images of DAPI staining of intestinal nuclei (denoted by red arrowhead) in N2 and *xpf-1* mutant animals fed with L4440 RNAi. (**F**) Immunoblots of histone H4K16ac (left) and its quantitation relative to β-actin (right) in N2 and *xpf-1* treated with L4440 or *acs-2* RNAi. $n = 3$. Data are means ± SD, two-tailed Student's *t* test. Representative images of DAPI staining of intestinal nuclei (denoted by red triangle) (**G**) and quantitation of its cross-sectional area in N2 and *xpf-1* mutant animals fed with L4440 or *acs-2* RNAi (**H**). Scale bars, 25 μm. The area with green dotted line or asterisk denotes nuclei of germ cells. $n = 40$ for N2 and *xpf1* (control), 12 for N2 (*acs-2*), and 18 for *xpf-1* (*acs-2*). Data are means ± SD, two-way ANOVA, Tukey's test. (**I**) Relative mRNA levels (from qPCR) of CYP genes in N2 and *xpf-1*. $n = 5$ biological replicates. Data are means ± SD, two-way ANOVA, Sidak correction. All experiments were performed with D7 worms. AU, arbitrary units.

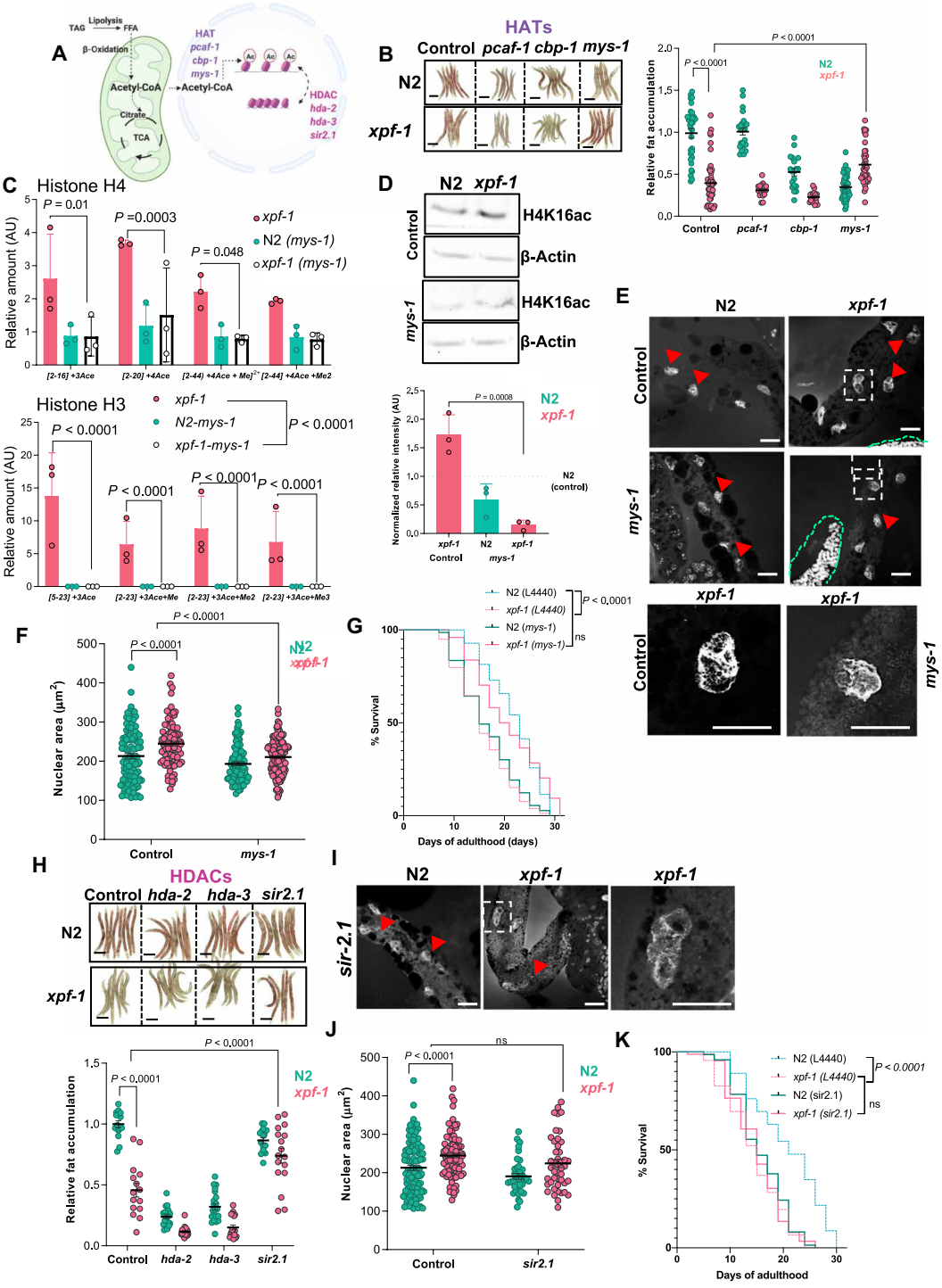

Fig. 5. MYS-1 and Sir2.1 control histone hyperacetylation in response to persistent DNA damage. (**A**) Acetylation and deacetylation of histones by HATs and HDACs. (**B**) Representative images and quantitation of fat depots by ORO staining in N2 and *xpf-1* animals fed with L4440 and *pcaf-1*, *cbp-1*, or *mys-1* HAT RNAi. Data are means ± SD. Two-way ANOVA, Tukey's test. Scale bars, 200 μM. (**C**) Relative levels of hyperacetylated peptides in Histone H4 (top) and H3 (bottom) measured using BAMS. (**D**) Immunoblots of H4K16ac in N2 and *xpf-1* animals fed with L4440 and *mys-1* RNAi. Quantitation of histone H4K16 levels relative to β-actin (bottom). $n = 3$. Data are means ± SD. (**E**) Representative image of DAPI staining of intestinal nuclear (pointed out by red triangle) cross-sectional area in N2 and *xpf-1* with L4440 and *mys-1* RNAi and (**F**) quantitation. Data are means ± SD. Two way ANOVA, Tukey's test. (**G**) Lifespan survival of N2 and *xpf-1* with L4440 and *mys-1* RNAi. Log-rank (Mantel-Cox) test. (**H**) Representative images and quantitation of lipid stores by ORO staining in N2 and *xpf-1* with L4440 and *hda-2*, *hda-3*, and *sir2.1* HDAC RNAi. Data are means ± SD, two-way ANOVA, Tukey's test. Scale bars, 200 μM. (**I**) Representative image of DAPI staining of intestinal nuclear cross-sectional area (pointed out by red triangle) in N2 and *xpf-1* fed with *sir-2.1* RNAi and (**J**) quantitation. Data are means ± SD, two-way ANOVA, Tukey's test. (**K**) Lifespan survival of N2 and *xpf-1* with L4440 and *sir-2.1* RNAi. Log-rank (Mantel-Cox) test. All experiments except lifespan were performed with D7 worms.

lifespan of *xpf-1* mutants (Fig. 5K). Overall, these results indicate that an increase in β-oxidation is tightly coupled with histone hyperacetylation, and this contributes to aging in response to persistent DNA damage.

Lipidome changes in *xpf-1* worms

Thus far, our data suggest that persistent DNA damage rewires lipid metabolism to promote histone hyperacetylation through MYS-1. Furthermore, we observed transcriptional up-regulation of CYP genes and an accumulation of PUFAs. CYPs can act on PUFAs and generate bioactive lipids (*40*). Therefore, we closely examined the lipidome alterations to identify bioactive lipid species in *xpf-1* mutants. We performed untargeted lipidomic profiling of N2, *xpf-1* worms treated with and without *mys-1* RNAi. Using a reversed-phase HR-LC–tandem MS (HR-LC-MS/MS), we identified 12 lipid classes. Negative ion mode was used to identify most of the PLs including oxidized PLs, as well as free fatty acids and oxidized free fatty acids (Fig. 6A), whereas positive ion mode was used to quantify the triacylglycerol (TAG) species. In total, we identified 793 lipid species including 354 TAG species and 175 oxidized free fatty acid species. Among PLs, 57 phosphatidyl ethanolamines, 52 cardiolipins, 47 phosphatidylcholines, and 23 lysophospholipids were identified (Fig. 6B). As expected, knockdown of *mys-1* in *xpf-1* mutants restored TAG levels (Fig. 6C). Similarly, PUFAs such as AA and EPA that were elevated in *xpf-1* were substantially reduced after *mys-1* knockdown (Fig. 6D). Since PUFAs are susceptible to lipid peroxidation, we next specifically examined for oxidized free fatty acids. Oxidized fatty acid species (~61%) were significantly elevated in *xpf-1* mutants, suggesting an increase in lipid oxidation in *xpf-1* mutants (Fig. 6E, top). However, upon *mys-1* knockdown, 57% oxidized fatty acids were significantly decreased in *xpf-1* mutants (Fig. 6E, bottom). These oxidized fatty acids were initially identified on the basis of the exact mass, retention time, and its ability to lose CO_2 during fragmentation analysis. Subsequent fragmentation analysis and comparison with standards revealed that the three prominent lipid mediators, prostaglandin E2, 11,12-EpTrE (11, 12-epoxy-eicosatrienoic acid), and leukotriene B4, were elevated in *xpf-1* mutants (Fig. 6F). *C. elegans* lack lipid-oxidizing enzymes such as lipoxygenases and cyclooxygenases; however, several oxidized free fatty acids including prostaglandins have been reported in these models. Studies suggest that CYP genes are involved in the synthesis of oxidized fatty acids in worms (Fig. 6G). Thus, we hypothesized that the up-regulation of CYP genes in *xpf-1* mutants is regulated by *mys-1*–mediated histone hyperacetylation and gene transcription. Upon *mys-1* knockdown worms, the levels of *clec* and *cyp* gene expression are comparable in N2 and *xpf-1* mutants and correlate to the decrease in lipid mediators (Fig. 6, E and H, and fig. S6C).

Phospholipids are the major sources for PUFAs in biological system. Since we observed significant changes in free PUFA and oxidized fatty acids levels, we then analyzed the phospholipidome of *xpf-1* mutant. Most of the PUFAs containing phosphatidylcholines and phosphatidylethanolamines were significantly decreased in *xpf-1* mutants. In addition, the levels of all identified lysophosphotidyl ethanolamine species were decreased in *xpf-1* mutants. On the other hand, levels of phosphatidylinositol were increased in *xpf-1* mutants, suggesting alterations in PL metabolism in these mutants. Knockdown of *mys-1* in *xpf-1* mutants significantly increased several prominent SFAs and MUFAs containing PE species such as 30:0, 32:0, 30:1, 38:1, and 38:2, whereas levels of predominant PUFAs containing PE species such as 36:5, 38:5, 40:5, 38:6, and 40:6 were significantly reduced (Fig. 6I). Together, these results suggest that suppression of *mys-1* during persistent DNA damage facilitates a reduction in oxidizable lipid substrates. Sphingomyelins are another category of lipids that showed differences in *xpf-1* after *mys-1* treatment. All sphingomyelin species were elevated in *xpf-1* mutant, while *mys-1* treatment decreased all but one species (SM 32:0) (fig. S7). Overall, these findings revealed that persistent DNA damage caused a global shift in lipid metabolism with the most significant alterations occurring in TAGs and free PUFAs.

DISCUSSION

In this study, we describe a mechanism through which persistent DNA damage alters the metabolic-epigenetic axis and promotes an immune-like response (Fig. 7). We show that persistent DNA damage reprograms metabolism to mitochondrial β-oxidation for generating acetyl-CoA. This acetyl-CoA promotes aberrant histone hyperacetylation, chromatin opening, and subsequent expression of immune-effector genes. Furthermore, our data indicate that persistent DNA damage–driven metabolic rewiring increases free PUFAs that can be metabolized by the CYP gene family resulting in proinflammatory lipid mediators. The HAT, *mys-1,* is responsible for the persistent DNA damage–driven epigenome alterations and age-related decline.

Fat storage and breakdown plays an important role in maintaining health. In humans, excessive fat depots are usually associated with chronic disease. However, several studies also point to the fact that loss of fat stores is an important risk factor in older adults. It is associated with frailty, higher hospital admissions, functional decline, and poor quality of life (*41*, *42*). Increase in fat storage has also been associated with longevity in both invertebrates and mammals (*30*). Several animal models with persistent DNA damage have loss of fat depots, consistent with our results (*16*, *17*, *43*, *44*). Here, we provide mechanistic insights into how depleted fat depots are a by-product of excessive β-oxidation, and inhibition of this process is beneficial in the context of persistent DNA damage.

Emerging evidence shows that nuclear DNA damage and metabolism are inextricably linked (*44*). Acute genotoxic stress tightly and transiently coordinates metabolic events to promote repair and maintain homeostasis (*9*). However, the cellular and metabolic events in response to persistent DNA damage are only recently being explored. Persistent DNA damage in the liver and hepatocytes of $Ercc1^{-/\Delta}$ mice was shown to inhibit glycolysis and favored reduced form of nicotinamide adenine dinucleotide phosphate production through the pentose phosphate shunt (*45*). A recent study also showed that in response to both acute and persistent genotoxic stress, an increase in mitochondrial β-oxidation feeds into oxidative phosphorylation in a cell-autonomous manner (*17*). In this study, inhibition of β-oxidation through the CPT inhibitor, etomoxir, seemed to have detrimental effects. However, it is important to note that, in this case, etomoxir treatment was performed after an acute exposure to an exogenous DNA damaging agent. These data suggest that upon acute exposure to DNA damage, a transient shift toward β-oxidation is beneficial and required for DNA repair. In contrast, during persistent DNA damage, our study shows that genetic inhibition of mitochondrial β-oxidation in DNA repair–deficient animals restored fat depots, suppressed histone hyperacetylation, and extended lifespan. Therefore, in the context of persistent DNA damage that occurs with age, maintaining β-oxidation could be detrimental.

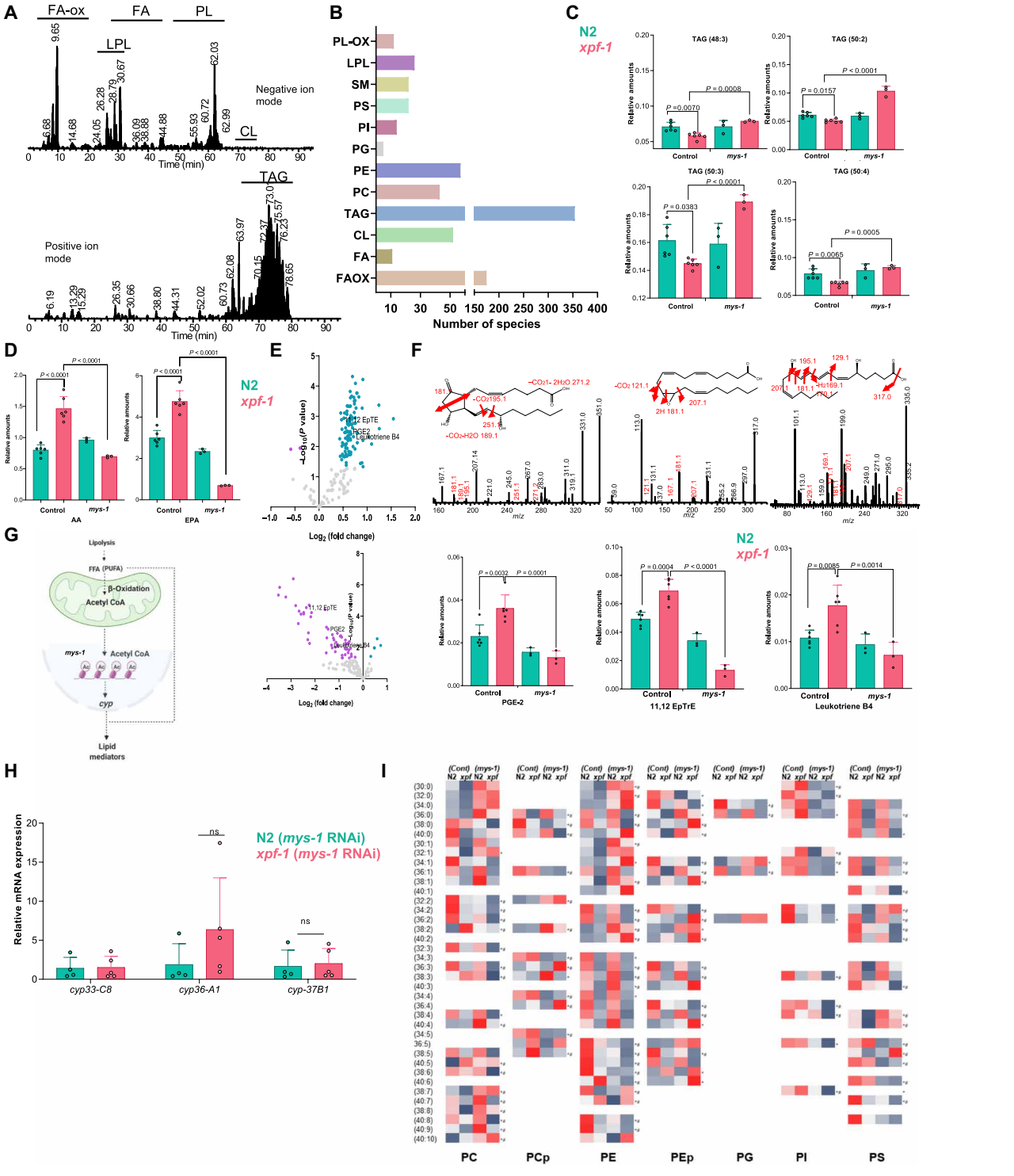

Fig. 6. Persistent DNA damage increases lipid mediators. (**A**) Extracted ion chromatography from LC-MS/MS of *C. elegans* (N2) in negative ion mode (top) and positive ion mode (bottom). (**B**) Bar graph showing number of species identified in each lipid categories. Bar graphs showing levels of major triacylglycerol species that were significantly reduced in *xpf-1* mutants and restored upon knocking down *mys-1* (**C**), AA and EPA (**D**) in N2, *xpf-1* worms with and without *mys-1* RNAi. Data are means ± SD, two-way ANOVA, Tukey's multiple comparison test. (**E**) Volcano plot showing the differences in oxidized free fatty acid levels in *xpf-1* versus N2 worms (top) and *xpf-1*(*mys-1 RNAi*) versus *xpf-1* control worms. (**F**) Distribution of three lipid mediators prostoglandin-E2, 11 to 12 EpTrE, and leukotriene B4 identified in the *C. elegans* lipidome (bottom) and its fragmentation spectrum of data are means ± SD. Two-way ANOVA, Tukey's test. (**G**) Working model showing excess β-oxidation drives histone hyperacetylation and production of lipid mediators in *xpf-1*. (**H**) Levels of *cyp* genes in N2(*mys-1 RNAi*) and *xpf-1*(*mys-1 RNAi*) worms measured by qRT-PCR. Data are means ± SD, two-way ANOVA, Tukey's test. (**I**) Heatmap showing the distribution of PLs in N2, *xpf-1*, N2(*mys-1*), and *xpf-1*(*mys-1*) worms. *$P < 0.05$, *xpf-1* versus N2; #$P < 0.05$, *xpf-1*(*mys-1*) versus *xpf-1*. Student's *t* test $n = 6$ for N2, *xpf-1* and 3 for N2(*mys-1 RNAi*) and *xpf-1*(*mys-1 RNAi*). All lipid data presented in this figure are from lipidomics analysis from D7 worms.

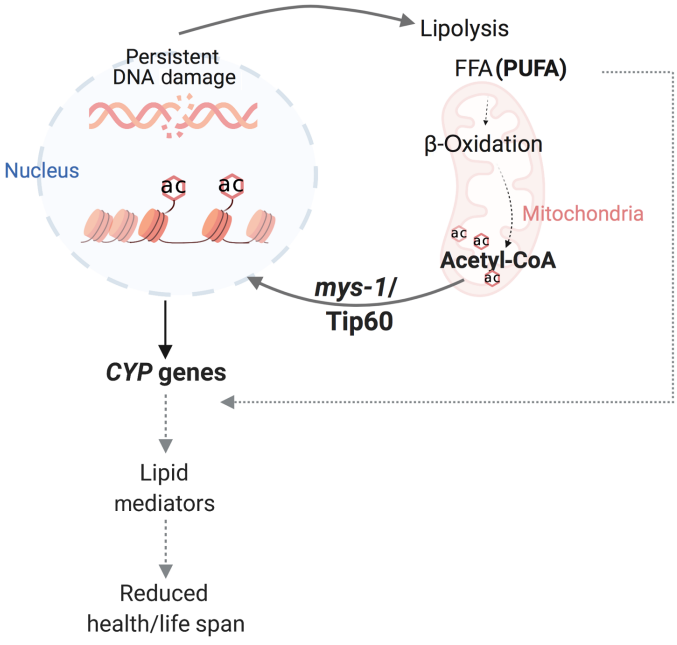

Fig. 7. Working model. Persistent DNA damage drives increased mitochondrial β-oxidation to generate a critical metabolite, acetyl-CoA. Acetyl-CoA is used by the histone acetyltransferase (HAT), *mys-1* (Tip60), to promote histone hyperacetylation leading to transcription of immune-effector genes/ CYPs. PUFAs, such as AA can be acted upon by CYPs to generate AA-related lipid mediators and promote a "proinflammatory signature," thus affecting health and lifespan.

Several studies show that specific inhibition of mitochondrial β-oxidation significantly reduces acetyl-CoA levels, while basal mitochondrial respiration and ATP remain unaffected (*46*, *47*). Moreover, a recent study showed that lipid-derived acetyl-CoA is mostly responsible for histone acetylation, chromatin regulation, and gene transcription (*33*). Consistent with this, we observed that the increased mitochondrial β-oxidation was intimately linked with histone hyperacetylation. Emerging evidence supports a role for histone acetylation in aging. For example, H4K16ac accumulates during yeast replicative aging (*48*) and leads to a loss of H4 histone in proliferating cells. Although we did observe an increase in histone acetylation, this was not associated with a general loss of histones in DNA repair–deficient mutant *C. elegans*. H4K16ac has also been observed in aging brains, but a decrease in this histone mark was associated with an age-related pathology, Alzheimer's disease, suggesting that it is critical to have an in-depth understanding of both global and local changes of these histone modifications. Future studies to discern the distribution of this histone acetylation mark needs to be performed to understand how it contributes to age-related decline. Consistent with this, overexpression of the sirtuin family of HDACs have long been linked to longevity (*49*). These studies suggest that histone hyperacetylation may have a causal role in promoting biological aging. Our study now provides a link between histone hyperacetylation and an increase in chronic immune–like response.

Since persistent DNA damage drives rewiring of lipid metabolism, we comprehensively analyzed lipid alterations in this context. The levels of two related lipid classes, free PUFAs and oxidized free fatty acids, correlate with the lifespan of *C. elegans*. Both of these lipids were elevated in the short-lived *xpf-1* mutants but reduced upon knockdown of *mys-1*, suggesting that the HAT, MYS-1, is the regulator of the metabolic-epigenetic axis in response to persistent DNA damage. A general consensus is that the higher ratio of MUFA-to-PUFA is crucial in maintaining healthy lifespan (*50*). Supplementation and genetic modification of PUFA-producing enzymes support this notion (*30*, *51*, *52*). In our study, the MUFA/PUFA ratio in the free fatty acid pools decreased markedly, while changes in the esterified forms were negligible. This suggests that free fatty acids are likely more capable of regulating lifespan than the esterified forms. Among PUFAs, generally ω-3 PUFAs such as ALA and EPA are beneficial (*52*), while ω-6 PUFAs are often detrimental. Most of the oxidized free fatty acids derived from ω-6 PUFAs are proinflammatory lipid mediators, which leads to a decline in cell function or to cell death (*53*). In contrast, most of the lipid mediators derived from ω-3 fatty acids signal anti-inflammatory events and are prosurvival signals (*54*).

In DNA repair–deficient mutants, we observed an increase in CYP genes. While *cyp* genes are usually involved in xenobiotic and endobiotic response, in the presence of free PUFAs, they can exhibit dichotomous roles due to their ability to produce proinflammatory lipid mediators (*55*). With persistent DNA damage, we observed elevated levels of PUFAs, suggesting that the increased oxidized fatty acids are through the enzymatic action of CYPs on PUFA. Although both ω-3 and ω-6 PUFAs are elevated in *xpf-1* mutants, ~95% of the elevated lipid mediators are derived from the ω-6 PUFA, AA. Together, the results indicate a proinflammatory condition in *xpf-1* mutants. Whether these AA-derived lipid mediators directly affect lifespan needs to be further examined. Furthermore, the transcriptomic analysis also showed elevation of several immune response–like genes involved in innate immunity, possibly leading to a scenario of chronic inflammation. Several studies report that genes known to be up-regulated with mammalian aging include immunity and stress response genes (*56*, *57*). Constitutive up-regulation of immunity genes has been shown to promote "accelerated aging" phenotypes (*58*, *59*). There is accumulating evidence that suggests that persistent DNA damage leads to increased inflammation, and blunting this immune response is beneficial for health (*16*, *55*). Our multiomic study has now explored the interdependence of the metabolic, epigenomic, and inflammatory changes. Our data suggest that the shift in metabolism to β-oxidation, which leads to loss of fat depots, is causal to drive expression of immune response–like genes.

This study presents a few intriguing questions that needs to be investigated further. Previous studies have documented that local nuclear acetyl-CoA are required for histone acetylation (*34*). However, the mechanisms behind the export of β-oxidation–derived acetyl-CoA from mitochondria to the nucleus are unknown. One mechanism is via ACLY. However, supplementation of citrate, as well as knockdown of *acly-1* and *acly-2*, did not restore fat reserves in the *xpf-1* mutant, indicating that this route is not engaged under persistent DNA damage conditions. Furthermore, studies have suggested that acetyl-carnitines from acetyl-CoAs are transported from mitochondria into the nucleus (*35*). Further studies to investigate both subcellular pools of acetyl CoA and related metabolites, as well as the "shuttle proteins" involved in the transport of acetyl CoA, will be very informative. Second, are there any other alternative routes that are responsible for hyperacetylation in addition to β-oxidation? One alternative route could be the mitochondrial propionate shunt, in which propionyl-CoA is converted to acetyl-CoA. Propionyl-CoA is synthesized via β-oxidation or oxidation of methionine, valine, isoleucine, and threonine. Propionate shunt is catalyzed by acdh-1 (*60*). In *xpf-1* mutants, we observed elevated levels of propionyl-carnitines,

valine, and *acdh-1*. Furthermore, knockdown of *acdh-1* rescued fat loss. These findings show that, in addition to β-oxidation, the propionate shunt may be involved in DNA damage–related histone hyperacetylation.

Our findings provide a missing link between metabolic rewiring, epigenetic modification, and aging in response to persistent DNA damage. Our results indicate that perturbation of any one of the three interconnected cellular processes—metabolism, epigenetic modification, and lipid oxidation—is enough to rescue the deleterious effects of persistent DNA damage. Future studies could target any one of these pathways or collectively all these pathways to ameliorate chronic DNA damage–associated health decline. These strategies could include dietary supplementation of less oxidizable fatty acids such as MUFA, providing alternative acetyl-CoA substrates such as acetate or using pharmacological inhibitors of lipid oxidation.

MATERIALS AND METHODS

C. elegans maintenance and strains

C. elegans were grown at 20°C on nematode growth medium (NGM) agar plates seeded with *Escherichia coli* OP50 or HT115, unless specified. All strains were extensively backcrossed (~5 to 10 times). Fresh stock was thawed every 3 months, and PCR was used to confirm genotype. *E. coli* OP50 was cultured overnight in LB at 37°C. *E. coli* HT115 was used to perform RNAi and was cultured overnight at 37°C in LB containing ampicillin (100 μg/ml). N2 Bristol was used as the wild-type strain. All strains were provided by the Caenorhabditis Genetics Centre Strains used in this study are listed in table S3.

ORO staining

ORO staining was performed as described previously (*25*). Briefly, ~80 to 150 adult animals at indicated ages were washed three times with 1× phosphate-buffered saline (PBS) (pH 7.4). To permeabilize the cuticle, worms were resuspended in 120 μl of PBS to which an equal volume of 2× Modified Ruvkun's Witches Brew (MRWB) buffer containing 2% paraformaldehyde (PFA) was added. The 2× MRWB buffer contains the following 160 mM KCl, 40 mM NaCl, 14 mM Na_2EGTA, 1 mM spermidine-HCl, 0.4 mM spermine, 30 mM Na-Pipes (pH 7.4), and 0.2% ß-mercaptoethanol. Samples were gently rocked for 1 hour at room temperature. Animals were allowed to settle by gravity, buffer was aspirated, and worms were washed with 1× PBS to remove PFA. Worms were then resuspended in 60% isopropanol and incubated for 15 min at room temperature to dehydrate. ORO is prepared as follows: A 0.5 g/100 ml isopropanol stock solution equilibrated for several days was freshly diluted to 60% with water and rocked for at least 1 hour and then filtered with 0.45- or 0.22-μm filter. After allowing worms to settle, isopropanol was removed, 120 μl of 60% ORO stain was added, and animals were incubated overnight with rocking. Unbound dye was removed after allowing worms to settle, and adding 240 μl of 1× PBS 0.01% Triton X-100 was added. The worms were washed two times with 1× PBS (pH 7.4). Animals were mounted on 2% agarose pads.

ORO quantification

ORO worms were imaged at 10× magnification using an ECHO Revolve microscope and saved as TIF files. The same exposure settings were used across all conditions within each experiment. Using Cell Profiler processing software, raw images were inverted, separated into RED, GREEN, and BLUE, and thresholded to outline the worm body (*61*). The same threshold values were used across all conditions within each experiment. Oil red staining inside worms is then identified using a threshold value using inverted BLUE channel. The threshold values were uniform across all analysis. The area of the worm and the ORO-stained area of each worm was calculated. The data are represented as a fraction of ORO-stained area to the total worm area. To normalize for experimental batch variations, each experiment carried control groups (L4440-N2), and all data are normalized to the average value of the control group. The data (arbitrary units) were graphed using GraphPad Prism, and statistical significance was determined two-way analysis of variance (ANOVA) with Sidak multiple comparison test.

Lipid analysis

Triacylglycerol levels were quantified using the Biovision Kit for TAG assay Triacyl glyceride quantification kit as described with a few modifications (*62*). Briefly, 2000 worms in the mentioned stage were collected washed with M9 buffer. The worms were then transferred to Precellys hard tissue homogenizing (2 ml) tubes with 100 μl of water and lysed using two times for 20-s lysis at 6800 rpm setting. After the lysis, 100 μl of 10% NP-40 alternative was added, and the sample was heated to 100°C in water bath for 5 min and cooled down to room temperature. Boiling of the sample was repeated once again, and the samples were centrifuged for 2 min at 1200*g*. The supernatants were collected, and the TAG amounts were measured using the manufacture's protocol.

Total lipids for PL analysis and lipidomics were extracted using the folch lipid extraction protocol. Briefly, 2000 worms were lysed in 500 μl of 0.75% KCL solution using the Precellys homogenizer. Three milliliters of 2:1 chloroform methanol was added to the homogenized solution and incubated for 1 hour with vigorous shaking at 4°C. Samples were centrifuged at 3000*g* for 10 min at 4°C for phase separation and organic layers were separated. To the aqueous and protein layers, 2 ml of chloroform was added and the lipids were reextracted. Both organic layers were pooled together, dried under nitrogen, and resuspended in 100 μl of 2:1 chloroform methanol containing 0.1% butylated hydroxytoluene (BHT). Total PLs were quantified using a micro method for phosphorus (*63*).

Quantitative RT-PCR

For experiments using whole worms, at least 500 age-synchronized worms in biological triplicate for each condition were harvested, washed three times with M9, and resuspended in 500 μl of TRIzol. To extract total RNA, worm or tissue pellets in TRIzol underwent six freeze-thaw cycles in a dry ice-ethanol bath. RNA was extracted according to the TRIzol procedure and resuspended in ribonuclease (RNase)– and deoxyribonuclease-free water. RNA from whole worms was quantified using the Qubit 2.0 fluorometer (Invitrogen), and at least 500 ng of total RNA per condition was used for cDNA synthesis (*29*). Total RNA was then reverse-transcribed using the Transcriptor First Strand cDNA Synthesis Kit (Roche), based on the manufacturer's instructions. RT-qPCR was performed using diluted cDNA on a Quantsudio3 (Applied Biosystems) with PowerUp SYBR green (Invitrogen). Primers used in RT-qPCR are listed in table S2. Melt curves were examined to ensure primer specificity. Results were analyzed using the standard $\Delta\Delta C_T$ method, and values were normalized to *rpl-32* or *act-1* as an internal control. All data shown represent at least three biologically independent samples.

Lifespan analysis

Worms were age-synchronized by egg-lay. For all experiments, every genotype and condition was performed in parallel at 20°C. Worms were transferred to RNAi plates as D1 (day 1) adults. To prevent progeny production, during adulthood, worms were transferred to FUDR-containing NGM (2.5 μg/ml) seeded plates every 2 days. Sixty to 100 animals were assayed for each condition per genotype. Worms were scored every second day. Death was indicated by total cessation of movement in response to gentle mechanical stimulation (*20*). Prism6 software was used for statistical analysis. Log-rank (Mantel-Cox) method was used to determine the significant difference.

Intestinal nuclei analysis

Dissection and fixation were carried out by freeze-crack method (*64*). Worms were dissected in M9 buffer on a polylysine-coated slide. The slides were fixed in ice-cold ethanol for 2 min. Next, the slides were placed in PBS and washed with fresh PBS for 5 min. Slides were then mounted with DAPI solution (VECTASHIELD). We used at least 30 worms in each sample for DAPI staining, and intestinal nuclei from more than 10 worms were selected and quantified for nuclear size (*64*).

Image analysis of intestinal nuclei

Intestinal cells were imaged at ×63 magnification using a Leica-TCS SP8 laser scanning confocal microscope. Z-stacks of the intestine were analyzed using LAS X. Contours of individual nuclei, according to DAPI fluorescence, were manually defined and used to render nuclei area. Maximum cross-sectional area of each nucleus was acquired from the surface tool statistics by ImageJ.

Western blot analysis

Age-synchronized worms ~1500 were washed off from the plate with M9 buffer and frozen in liquid nitrogen. Equal volume of sample buffer [0.1 M tris (pH 6.8), 7.5 M urea, 2% SDS, 100 mM β-mercaptoethanol (β-ME), and 0.05% bromophenol blue] was added to worms. Worm extracts were generated by sonication by heating worms to 65°C for 10 min, sonicating for two 30-s bursts, heating to 95°C for 5 min and then kept at 37°C until loading onto SDS–polyacrylamide gel electrophoresis gel (*65*). Proteins were transferred to nitrocellulose and blotted with the following antibodies: H4K16ac (active motif 39930) at 1:1000, and β-actin (Sigma-Aldrich, A3854) at 1:1000.

Compound treatment assay

Pyruvate, acetate, and citrate treatment

We performed metabolite treatment assays by adding pyruvate, acetate, and citrate to a final concentration of 50 mM on the NGM plates (*64*). Worms were transferred on compound plates with FUDR as day 1 adults and transferred every day until D7.

Transcriptomics

Sample preparation

At least 500 age-synchronized worms in biological triplicate for each condition were harvested, washed five times with M9, and resuspended in 500 μl of TRIzol. RNA extraction was carried out as mentioned above.

RNA quantification and qualification

RNA degradation and contamination was monitored on 1% agarose gels. RNA purity was checked using the NanoPhotometer spectrophotometer (IMPLEN, CA, USA). RNA integrity and quantitation were assessed using the RNA Nano 6000 Assay Kit of the Bioanalyzer 2100 system (Agilent Technologies, CA, USA).

Library preparation for transcriptome sequencing

A total amount of 1 μg of RNA per sample was used as input material for the RNA sample preparations. Sequencing libraries were generated using the NEBNext Ultra RNA Library Prep Kit for Illumina [New England Biolabs (NEB), USA] following manufacturer's recommendations, and index codes were added to attribute sequences to each sample. Briefly, mRNA was purified from total RNA using poly-T oligo–attached magnetic beads. Fragmentation was carried out using divalent cations under elevated temperature in NEB Next First Strand Synthesis Reaction Buffer (5×). First strand cDNA was synthesized using random hexamer primer and M-MuLV Reverse Transcriptase (RNase H-). Second strand cDNA synthesis was subsequently performed using DNA Polymerase I and RNase H. Remaining overhangs were converted into blunt ends via exonuclease/polymerase activities. After adenylation of 3′ ends of DNA fragments, NEB Next Adaptor with hairpin loop structure was ligated to prepare for hybridization. To select cDNA fragments of preferentially 150 to 200 base pairs (bp) in length, the library fragments were purified with AMPure XP system (Beckman Coulter,Beverly, USA). Then, 3 μl of USER Enzyme (NEB, USA) was used with size-selected, adaptor-ligated cDNA at 37°C for 15 min followed by 5 min at 95°C before PCR. Then, PCR was performed with Phusion High-Fidelity DNA polymerase, Universal PCR primers and Index (X) Primer. Last, PCR products were purified (AMPure XP system) and library quality was assessed on the Agilent Bioanalyzer 2100 system.

Clustering and sequencing

The clustering of the index-coded samples was performed on a cBot Cluster Generation System using the PE Cluster Kit cBot-HS (Illumina) according to the manufacturer's instructions. After cluster generation, the library preparations were sequenced on an Illumina platform, and 125/150 bp paired-end reads were generated.

Quality control

Raw data (raw reads) of fastq format were first processed through in-house (by Novogene) perl script. In this step, clean data (clean reads) were obtained by removing reads containing adapter, reads containing ploy-N, and low-quality reads from raw data. At the same time, Q20, Q30, and GC content for the clean data were calculated. All the downstream analyses were based on the clean data (with high quality).

Reads mapping to the reference genome

Reference genome and gene model annotation files were downloaded from genome website directly. The reference genome is WBcel235 (genome-date 2012-12 genome-build-accession NCBI:GCA_000002985.3 genebuild-last-updated 2014-02), annotated features correspond to WormBase release WS281. Index of the reference genome was built using hisat2 2.1.0, and paired-end clean reads were aligned to the reference genome using HISAT2. We selected HISAT2 as the mapping tool for that Hisat2 can generate a database of splice junctions based on the gene model annotation file and thus a better mapping result than other nonsplice mapping tools, which is a fast and sensitive alignment program for mapping next-generation sequencing reads against the general human population.

Quantification of gene expression level

Feature Counts v1.5.0-p3 was used to count the reads numbers mapped to each gene (*66*). Then, the FPKM of each gene was calculated on the basis of the length of the gene and reads count mapped to this gene. FPKM, expected number of fragments per kilobase of transcript sequence per million base pairs sequenced, considers the

effect of sequencing depth and gene length for the reads count at the same time and is currently the most commonly used method for estimating gene expression levels (*67*).

Differential expression analysis

Differential expression analysis was performed using the DESeq2 R package (1.14.1). DESeq2 provide statistical routines for determining differential expression in digital gene expression data using a model based on the negative binomial distribution. The resulting *P* values were adjusted using the Benjamini and Hochberg's approach for controlling the false discovery rate. Genes with an adjusted *P* value < 0.05 found by DESeq2 were assigned as differentially expressed. Pathway enrichment analysis was performed using Wormcat online tool as described in Holdorf *et al.* (*23*). Figures from the data were generated using ggplot2 or R language.

Metabolomics

Sample preparation

A synchronous population of 500 day 7 worms were washed off the plates in M9 buffer and collected in 1.5-ml Eppendorf tubes. The worms were further washed three times with 0.5 ml of mass-spec grade water. After the final wash, the worms were collected in 0.5-ml of ice-cold 80% methanol into 2-ml homogenizer tubes. The worms were homogenized with a 5-mm steel bead using a TissueLyser II (Qiagen) for 2 × 2.5 min at a frequency of 30 times/s, followed by a tip sonication (energy level: 40 J; output: 8 W) for two times on ice water. Samples were centrifuged at 14,000 rpm and 4°C for 10 min, the supernatant was transferred to a fresh Eppendorf tube, and the solvent was removed. The residue was dissolved in 100 μl of MeOH and transferred to an autosampler vial following centrifugation to remove any particulate matter.

Untargeted high-resolution LC-HRMS

Sample preparation

Metabolic quenching and polar metabolite pool extraction were performed by adding ice-cold 80% methanol at a ratio of 1:15 weight:volume. Internal standards used: deuterated (D_3)-creatinine and (D_3)-alanine, (D_4)-taurine, (D_3)-lactate (Sigma-Aldrich) at a final concentration of 10 μM. Samples were homogenized for 40 s at 60 Hz using an MP Bio FastPrep with Matrix A beads. The supernatant was cleared of protein by centrifugation at 16,000*g*. Two microliters of cleared supernatant was subjected to online LC-MS analysis.

LC-HRMS method (polar)

Analyses were performed by untargeted LC-HRMS. Briefly, samples were injected via a Thermo Vanquish UHPLC and separated over a reversed-phase Thermo HyperCarb porous graphite column (2.1 mm by 100 mm, 3-μm particle size) maintained at 55°C. For the 20-min LC gradient, the mobile phase consisted of the following: solvent A (water/0.1% FA) and solvent B [ACN (Acetonitrile)/0.1% Formic acid (FA)]. The gradient was the following: 0- to 1-min 1% B, increase to 15% B over 5 min, continue increasing to 98% B over 5 min, hold at 98% B for 5 min, reequillibrate at 1% B for 5 min. The Thermo IDX tribrid mass spectrometer was operated in both positive and ion modes, scanning in $ddMS^2$ mode (two microscans) from 100 to 800 mass/charge ratio (*m*/*z*) at 70,000 resolution with an AGC target of 2×10^5 for full scan and 2×10^4 for ms^2 scans. Source ionization setting was 3.0- and 2.4-kV spray voltage, respectively, for positive and negative modes. Source gas parameters were 35 sheath gas, 12 auxiliary gas at 320°C, and 8 sweep gas. Calibration was performed before analysis using the Pierce FlexMix Ion Calibration Solutions (Thermo Fisher Scientific). Integrated peak areas of known identity from in-house libraires were then extracted manually using Quan Browser (Thermo Fisher Xcalibur ver. 2.7). Untargeted differential comparisons were performed using Compound Discoverer 3.0 (Thermo Fisher Scientific) to generate a ranked list of significant compounds with tentative identifications from BioCyc, Kyoto Encyclopedia of Genes and Genomes, and internal databases.

Data analysis

Levels of TCA metabolites, carnitine and acetyl-carnitine, and AA were quantified using Quan browser software. Untargeted analysis of metabolomics data was performed using compound discoverer software. Peaks with 10,000 ion intensity and 10 S/N (Signal-to-noise ratio) were identified, and various adducts are consolidated using *m*/*z* and the retention time. Compounds are then queried against PubChem and Human metabolomic database and MZ cloud fragmentation database to obtain putative identifications. Peaks with more than one identity is confirmed on the basis of manual fragmentation analysis. Data were then normalized on the basis of the internal standard analyzed using GraphPad Prism software. PCA analysis was performed using SIMCA software.

Transcriptomic and metabolomics data integration

Enriched transcriptomic and metabolomics data were used for transcriptomic data integration. List of enriched transcripts and metabolites were submitted to the MOFA2 software in R language (*24*). A model was developed with two factors. Both the metabolites and the transcript with the normalized future weight >1 were selected as the transcripts/metabolites with highly coordinated levels. These transcripts were then subjected to pathway enrichment analysis using wormcat as described previously (*23*).

Acetyl-CoA measurements

Two thousand worms were washed in 1× tris-buffered saline at least three times to get rid of bacteria. The worms were washed two times with sterile water, and then 1 ml of 10% ice-cold TCA (TCA solution in −20°C) was added. Then, the worms were collected in Precellys tubes and homogenized "hard" two times. The lysates were collected in prechilled 1.5-ml Eppendorf tubes and used for acetyl-CoA quantitation.

Acetyl-CoA was measured by HR-LC-MS as previously reported (*68*). Briefly, samples and calibrators generated from commercially available standards (from Sigma-Aldrich) were spiked with a constant amount of $^{13}C_3{}^{15}N_1$-acyl-CoA extract as an internal standard generated biosynthetically as previously described from $^{13}C_3{}^{15}N_1$-pantothenate (*69*). Samples were sonicated, then extracted by Oasis HLB solid phase extraction, evaporated to dryness, and resuspended in 50 μl of 5% 5-sulfosalicylic acid in water; and 10 μl was injected for analysis on a Ultimate 3000 UHPLC (Thermo Fisher Scientific) with a Waters HSS T3 column (2.1 mm by 100 mm) coupled to a Q Exactive Plus (Thermo Fisher Scientific) operating in positive ion mode alternating full scan from 760 to 1800 *m*/*z* at 140,000 resolution; and data-independent acquisition was looped three times with all fragment ions multiplexed at a normalized collision energy of 20 at a resolution of 280,000. Operating conditions on the mass spectrometer were as follows: auxiliary gas, 10 arbitrary units (arb); sheath gas, 35 arb; sweep gas, 2 arb; spray voltage, 4.5 kV; capillary temperature, 425°C; S-lens radio frequency (RF) level, 50; aux gas heater temperature, 400°C; in-source collision induced dissociation

(CID) 5 eV. LC conditions were column oven temperature at 30°C, solvent A water with 5 mM ammonium acetate, solvent B 95:5 acetonitrile:water with 5 mM ammonium acetate, and solvent C (wash solvent) 80:20 acetonitrile:water with 0.1% formic acid with the following gradient of 0.2 ml/min flow at 98% A and 2% B for 1.5 min, 80% A and 20% B at 5 min, and 100% B at 12 min; 0.3 ml/min at 100% B at 16 min; and 0.2 ml/min at 100% C at 17 min, held to 21 min, and then reequilibrated at 0.2 ml/min flow at 98% A and 2% B from 22 to 28 min. Flow from 4 to 18 min was diverted to the instrument. Data were processed in Xcalibur and TraceFinder 4.1 (Thermo Fisher Scientific). Protein normalization was by a Pierce BCA kit according to manufacturer's instructions.

Lipidomics

Lipidomics analysis was performed using HR-LC-MS/MS. Samples were analyzed using Dionex Ultimate 3000 HPLC system coupled on-line to a Q-Exactive Hybrid Quadrupole-Orbitrap Mass Spectrometer (Thermo Fisher Scientific). A reverse phase C30 column (Accucore C30; 2.6 μm, 150 Å, 250 mm by 2.1 mm; Thermo Fisher Scientific) and a binary gradient consisting of solvent A (1:1 acetonitrile:water with 0.1% formic acid and 5 mM ammonium formate) and solvent B (8.5:1:0.5 2-propanol:acetonitrile:water with 0.1% formic acid and 5 mM ammonium formate) were used for the chromatographic separation. Five nanomoles of PL samples was dried and dissolved in solvent B and injected in the LC using the autosampler. The following elution gradient was used: 0 to 20 min: an isocratic flow of 30% solvent B at 100 μl/min; 20 to 50 min: a liner gradient of 30 to 100% solvent B at a flow rate of 100 μl/min; 50 to 70 min: an isocratic flow of 100% solvent B at 100 μl/min; 70 to 85 min: linear gradient of 100 to 30% solvent B at 100 μl/min followed by 10-min reequilibration of column at 30% solvent B at 100 μl/min. The sample from LC was injected into the mass spectrometer using a heated electron spray ionization source. For PL analysis, the mass spectrometer was operated at negative ion mode with a spray voltage of 2.5 kV, capillary temperature of 320°C, sheath gas of 6 arb, S-lens RF of 60, mass range of 150 to 1800 *m*/*z* with a resolution of 70,000 Full width at half maximum (FWHM) at 200 *m*/*z*. MS/MS was performed on top 10 high ions using data-dependent mode. Higher-energy collisional dissociation method with 24% energy was used. For triacyl glycerol analysis, the mass spectrometer was operated in a positive ion mode with the spray voltage of 3.5 kV. Data were analyzed using Compound discoverer software as described previously (*70*). Identity of the lipids was confirmed by the representative fragmentation analysis. Statistical analysis was performed using GraphPad Prism software.

Identification of histone hyperacetylation by BAMS

Preparation of nuclei and digested peptides

Day 7 worms (2500) were pulverized under liquid nitrogen using a mortar and pestle for 5 min. The pulverized worms are then transferred to 200 μl of PBS and centrifuged at 14,000*g* for 5 min at 4°C. The pellets were resuspended in 10 volumes of nuclei isolation buffer [NIB; 15 mM tris-HCl (pH 7.5), 60 mM KCl, 15 mM $NaCl_2$, 1 mM $CaCl_2$, and 250 mM sucrose] supplemented with 1× halt protease inhibitors, 1 mM dithiothreitol (DTT), 10 mM sodium butyrate, and 0.3% NP-40. The suspension was incubated on ice for 30 min, followed by centrifugation at 600*g* for 5 min. The pellet was washed twice with 500 μl of NIB buffer. After washing, the pellet was suspended in 10 volumes of 1× micrococcal nuclease reaction buffer. Five microliters of the sample was aliquoted for protein measurement using the Bradford assay method. The remaining suspension was then subjected to sonication using a microtip for three bursts of 15 s each, followed by a 1-min cooling on ice. Following sonication, micrococcal nuclease was added at a ratio of 1:20 (enzyme:sample) and incubated at 37°C for 30 min. After the nuclease reaction, equal volumes of 0.2% Rapigest (Waters, Milford MA) in 100 mM ammonium bicarbonate were added, and the mixture was incubated at 80°C for 10 min. The samples were then cooled down to room temperature and treated with 5 mM DTT (final concentration) at 60°C for 30 min to reduce the disulfide bonds. The reduced samples are then alkylated using 10 mM (final concentration) iodoacetamide. One hundred micrograms of protein was then incubated overnight at 37°C with 2 μg of LysC. The protease was denatured by heating the sample at 80°C for 10 min.

Target peptide enrichment

Target peptide enrichment was performed using 100 μg of digested peptides with immune affinity beads. Peptides and affinity capture beads were incubated overnight at 4°C in an Eppendorf ThermoMixer. Beads were washed sequentially in PBS (700 μl), ammonium bicarbonate 700 μl, 10 mM, pH 8.0) and deionized water (700 μl) to remove any nonspecific bound peptides (2 min, 4°C). Washed BAMS beads are transferred to the hydrated wells and centrifuged (5 min, 200*g*) to settle into the microwells of the BAMS plate assembly with gentle agitation and centrifugation (5 min, 200*g*).After centrifugation, the sample chamber gasket is removed, leaving the microwell gasket fixed in place on the slide. The bead array is exposed to an aerosol of elution buffer using a Matrix Sprayer, containing α-cyano-4-hydroxycinnamic acid (0.5 mg/ml) in 50% acetonitrile and 0.4% trifluoroacetic acid for approximately 15 min. Once the matrix is dry, the silicone gasket is lifted off the slide, and any remaining dry agarose beads are removed by compressed air, leaving an array of spots containing purified and concentrated target peptides for subsequent matrix-assisted laser desorption/ionization (MALDI) MS measurement.

MALDI MS measurement

MALDI–time-of-flight (MALDI-TOF) MS data were acquired on a Bruker Daltonics (Billerica MA) rapifleX MALDI-TOF/TOF mass spectrometer using FlexControl software. The autoflex speed acquisition conditions in the positive linear mode were 700 to 7000 *m*/*z* mass range (2 kHz, 4000 spectra per spot using the random walk method). The voltage settings were 19.50 kV (ion source 1), 18.35 kV (ion source 2), and 6.0 kV (lens). The pulsed ion extraction was 130 ns. Mass spectra were processed and analyzed using FlexAnalysis software. Peaks were detected that had a signal-to-noise ratio of at least 3. The peaks were identified on the basis of their mass (table S4) and quantified on the basis of their intensity following blank subtraction. Peaks in the mass spectra are labeled using average *m*/*z* values using the peak picking algorithms available in the software.

Data deposition

RNA sequencing

RNA-seq data are available at www-ncbi-nlm-nih-gov.ezproxy.u-pec.fr/geo/query/acc.cgi?acc=GSE180506.

Untargeted metabolomics high-resolution LC-HRMS data

Untargeted metabolomics high-resolution LC-HRMS data are available at https://data.mendeley.com/datasets/hymdyg625p/draft?a=d4a95014-aad5-4e95-8f4a-bb52c95bc04c.

Untargeted high-resolution lipidomics data

Untargeted high-resolution lipidomics data are available at https://data.mendeley.com/v1/datasets/9dx3ysckgw/draft?a=be35a7fb-d86c-485d-ab7f-40a7f6a8525e.

SUPPLEMENTARY MATERIALS

Supplementary material for this article is available at https://science.org/doi/10.1126/sciadv.abl6083

View/request a protocol for this paper from *Bio-protocol*.

REFERENCES AND NOTES

1. B. Schumacher, J. Pothof, J. Vijg, J. H. J. Hoeijmakers, The central role of DNA damage in the ageing process. *Nature* **592**, 695–703 (2021).
2. L. J. Niedernhofer, A. U. Gurkar, Y. Wang, J. Vijg, J. H. J. Hoeijmakers, P. D. Robbins, Nuclear genomic instability and aging. *Annu. Rev. Biochem.* **87**, 295–322 (2018).
3. M. A. Lodato, R. E. Rodin, C. L. Bohrson, M. E. Coulter, A. R. Barton, M. Kwon, M. A. Sherman, C. M. Vitzthum, L. J. Luquette, C. N. Yandava, P. Yang, T. W. Chittenden, N. E. Hatem, S. C. Ryu, M. B. Woodworth, P. J. Park, C. A. Walsh, Aging and neurodegeneration are associated with increased mutations in single human neurons. *Science* **359**, 555–559 (2018).
4. I. Martincorena, J. C. Fowler, A. Wabik, A. R. J. Lawson, F. Abascal, M. W. J. Hall, A. Cagan, K. Murai, K. Mahbubani, M. R. Stratton, R. C. Fitzgerald, P. A. Handford, P. J. Campbell, K. Saeb-Parsy, P. H. Jones, Somatic mutant clones colonize the human esophagus with age. *Science* **362**, 911–917 (2018).
5. W. Wu, S. E. Hill, W. J. Nathan, J. Paiano, E. Callen, D. Wang, K. Shinoda, N. van Wietmarschen, J. M. Colón-Mercado, D. Zong, R. de Pace, H. Y. Shih, S. Coon, M. Parsadanian, R. Pavani, H. Hanzlikova, S. Park, S. K. Jung, P. J. McHugh, A. Canela, C. Chen, R. Casellas, K. W. Caldecott, M. E. Ward, A. Nussenzweig, Neuronal enhancers are hotspots for DNA single-strand break repair. *Nature* **593**, 440–444 (2021).
6. K. K. Ness, C. R. Howell, K. L. Bjornard, Frailty and quality of life in adult survivors of childhood cancer. *Expert Rev Qual Life Cancer Care* **2**, 79–85 (2017).
7. A. B. Smitherman, W. A. Wood, N. Mitin, V. L. Ayer Miller, A. M. Deal, I. J. Davis, J. Blatt, S. H. Gold, H. B. Muss, Accelerated aging among childhood, adolescent, and young adult cancer survivors is evidenced by increased expression of p16INK4aand frailty. *Cancer* **126**, 4975–4983 (2020).
8. S. Hayek, T. M. Gibson, W. M. Leisenring, J. L. Guida, M. M. Gramatges, P. J. Lupo, R. M. Howell, K. C. Oeffinger, S. Bhatia, K. Edelstein, M. M. Hudson, L. L. Robison, P. C. Nathan, Y. Yasui, K. R. Krull, G. T. Armstrong, K. K. Ness, Prevalence and predictors of frailty in childhood cancer survivors and siblings: A report from the childhood cancer survivor study. *J. Clin. Oncol.* **38**, 232–247 (2020).
9. S. Sivanand, S. Rhoades, Q. Jiang, J. V. Lee, J. Benci, J. Zhang, S. Yuan, I. Viney, S. Zhao, A. Carrer, M. J. Bennett, A. J. Minn, A. M. Weljie, R. A. Greenberg, K. E. Wellen, Nuclear acetyl-CoA production by ACLY promotes homologous recombination. *Mol. Cell* **67**, 252–265.e6 (2017).
10. A. Wilk, F. Hayat, R. Cunningham, J. Li, S. Garavaglia, L. Zamani, D. M. Ferraris, P. Sykora, J. Andrews, J. Clark, A. Davis, L. Chaloin, M. Rizzi, M. Migaud, R. W. Sobol, Extracellular NAD(+) enhances PARP-dependent DNA repair capacity independently of CD73 activity. *Sci. Rep.* **10**, 651 (2020).
11. W. P. Vermeij, M. E. T. Dollé, E. Reiling, D. Jaarsma, C. Payan-Gomez, C. R. Bombardieri, H. Wu, A. J. M. Roks, S. M. Botter, B. C. van der Eerden, S. A. Youssef, R. V. Kuiper, B. Nagarajah, C. T. van Oostrom, R. M. C. Brandt, S. Barnhoorn, S. Imholz, J. L. A. Pennings, A. de Bruin, Á. Gyenis, J. Pothof, J. Vijg, H. van Steeg, J. H. J. Hoeijmakers, Restricted diet delays accelerated ageing and genomic stress in DNA-repair-deficient mice. *Nature* **537**, 427–431 (2016).
12. M. Scheibye-Knudsen, S. J. Mitchell, E. F. Fang, T. Iyama, T. Ward, J. Wang, C. A. Dunn, N. Singh, S. Veith, M. M. Hasan-Olive, A. Mangerich, M. A. Wilson, M. P. Mattson, L. H. Bergersen, V. C. Cogger, A. Warren, D. G. le Couteur, R. Moaddel, D. M. Wilson III, D. L. Croteau, R. de Cabo, V. A. Bohr, A high-fat diet and NAD(+) activate Sirt1 to rescue premature aging in cockayne syndrome. *Cell Metab.* **20**, 840–855 (2014).
13. M. N. Okur, B. Mao, R. Kimura, S. Haraczy, T. Fitzgerald, K. Edwards-Hollingsworth, J. Tian, W. Osmani, D. L. Croteau, M. W. Kelley, V. A. Bohr, Short-term NAD(+) supplementation prevents hearing loss in mouse models of Cockayne syndrome. *NPJ Aging Mech Dis* **6**, 1 (2020).
14. F. Pietrocola, L. Galluzzi, J. M. Bravo-San Pedro, F. Madeo, G. Kroemer, Acetyl coenzyme A: A central metabolite and second messenger. *Cell Metab.* **21**, 805–821 (2015).
15. L. J. Niedernhofer, G. A. Garinis, A. Raams, A. S. Lalai, A. R. Robinson, E. Appeldoorn, H. Odijk, R. Oostendorp, A. Ahmad, W. van Leeuwen, A. F. Theil, W. Vermeulen, G. T. J. van der Horst, P. Meinecke, W. J. Kleijer, J. Vijg, N. G. J. Jaspers, J. H. J. Hoeijmakers, A new progeroid syndrome reveals that genotoxic stress suppresses the somatotroph axis. *Nature* **444**, 1038–1043 (2006).
16. I. Karakasilioti, I. Kamileri, G. Chatzinikolaou, T. Kosteas, E. Vergadi, A. R. Robinson, I. Tsamardinos, T. A. Rozgaja, S. Siakouli, C. Tsatsanis, L. J. Niedernhofer, G. A. Garinis, DNA damage triggers a chronic autoinflammatory response, leading to fat depletion in NER progeria. *Cell Metab.* **18**, 403–415 (2013).
17. L. E. Brace, S. C. Vose, K. Stanya, R. M. Gathungu, V. R. Marur, A. Longchamp, H. Treviño-Villarreal, P. Mejia, D. Vargas, K. Inouye, R. T. Bronson, C. H. Lee, E. Neilan, B. S. Kristal, J. R. Mitchell, Increased oxidative phosphorylation in response to acute and chronic DNA damage. *NPJ Aging Mech Dis* **2**, 16022 (2016).
18. A. Ahmad, A. R. Robinson, A. Duensing, E. van Drunen, H. B. Beverloo, D. B. Weisberg, P. Hasty, J. H. J. Hoeijmakers, L. J. Niedernhofer, ERCC1-XPF endonuclease facilitates DNA double-strand break repair. *Mol. Cell. Biol.* **28**, 5082–5092 (2008).
19. A. U. Gurkar, L. J. Niedernhofer, Comparison of mice with accelerated aging caused by distinct mechanisms. *Exp. Gerontol.* **68**, 43–50 (2015).
20. A. U. Gurkar, A. R. Robinson, Y. Cui, X. Li, S. K. Allani, A. Webster, M. Muravia, M. Fallahi, H. Weissbach, P. D. Robbins, Y. Wang, E. E. Kelley, C. M. S. Croix, L. J. Niedernhofer, M. S. Gill, Dysregulation of DAF-16/FOXO3A-mediated stress responses accelerates oxidative DNA damage induced aging. *Redox Biol.* **18**, 191–199 (2018).
21. L. Marchal, S. Hamsanathan, R. Karthikappallil, S. Han, H. Shinglot, A. U. Gurkar, Analysis of representative mutants for key DNA repair pathways on healthspan in Caenorhabditis elegans. *Mech. Ageing Dev.* **200**, 111573 (2021).
22. M. M. Mueller, L. Castells-Roca, V. Babu, M. A. Ermolaeva, R. U. Müller, P. Frommolt, A. B. Williams, S. Greiss, J. I. Schneider, T. Benzing, B. Schermer, B. Schumacher, DAF-16/FOXO and EGL-27/GATA promote developmental growth in response to persistent somatic DNA damage. *Nat. Cell Biol.* **16**, 1168–1179 (2014).
23. A. D. Holdorf, D. P. Higgins, A. C. Hart, P. R. Boag, G. J. Pazour, A. J. M. Walhout, A. K. Walker, WormCat: An online tool for annotation and visualization of Caenorhabditis elegans genome-scale data. *Genetics* **214**, 279–294 (2020).
24. R. Argelaguet, D. Arnol, D. Bredikhin, Y. Deloro, B. Velten, J. C. Marioni, O. Stegle, MOFA+: A statistical framework for comprehensive integration of multi-modal single-cell data. *Genome Biol.* **21**, 111 (2020).
25. E. J. O'Rourke, A. A. Soukas, C. E. Carr, G. Ruvkun, *C. elegans* major fats are stored in vesicles distinct from lysosome-related organelles. *Cell Metab.* **10**, 430–435 (2009).
26. S. S. Chirala, S. J. Wakil, Structure and function of animal fatty acid synthase. *Lipids* **39**, 1045–1053 (2004).
27. T. J. Brock, J. Browse, J. L. Watts, Fatty acid desaturation and the regulation of adiposity in Caenorhabditis elegans. *Genetics* **176**, 865–875 (2007).
28. Y. Li, W. Ding, C. Y. Li, Y. Liu, HLH-11 modulates lipid metabolism in response to nutrient availability. *Nat. Commun.* **11**, 5959 (2020).
29. P. V. Ramachandran, M. Savini, A. K. Folick, K. Hu, R. Masand, B. H. Graham, M. C. Wang, Lysosomal signaling promotes longevity by adjusting mitochondrial activity. *Dev. Cell* **48**, 685–696.e5 (2019).
30. S. Han, E. A. Schroeder, C. G. Silva-García, K. Hebestreit, W. B. Mair, A. Brunet, Mono-unsaturated fatty acids link H3K4me3 modifiers to *C. elegans* lifespan. *Nature* **544**, 185–190 (2017).
31. A. Folick, H. D. Oakley, Y. Yu, E. H. Armstrong, M. Kumari, L. Sanor, D. D. Moore, E. A. Ortlund, R. Zechner, M. C. Wang, Aging. Lysosomal signaling molecules regulate longevity in Caenorhabditis elegans. *Science* **347**, 83–86 (2015).
32. K. E. Wellen, G. Hatzivassiliou, U. M. Sachdeva, T. V. Bui, J. R. Cross, C. B. Thompson, ATP-citrate lyase links cellular metabolism to histone acetylation. *Science* **324**, 1076–1080 (2009).
33. E. McDonnell, S. B. Crown, D. B. Fox, B. Kitir, O. R. Ilkayeva, C. A. Olsen, P. A. Grimsrud, M. D. Hirschey, Lipids reprogram metabolism to become a major carbon source for histone acetylation. *Cell Rep.* **17**, 1463–1472 (2016).
34. L. Shi, B. P. Tu, Acetyl-CoA and the regulation of metabolism: Mechanisms and consequences. *Curr. Opin. Cell Biol.* **33**, 125–131 (2015).
35. P. Madiraju, S. V. Pande, M. Prentki, S. R. M. Madiraju, Mitochondrial acetylcarnitine provides acetyl groups for nuclear histone acetylation. *Epigenetics* **4**, 399–403 (2009).
36. G. G. Sharma, S. So, A. Gupta, R. Kumar, C. Cayrou, N. Avvakumov, U. Bhadra, R. K. Pandita, M. H. Porteus, D. J. Chen, J. Cote, T. K. Pandita, MOF and histone H4 acetylation at lysine 16 are critical for DNA damage response and double-strand break repair. *Mol. Cell. Biol.* **30**, 3582–3595 (2010).
37. G. M. Hamza, V. B. Bergo, S. Mamaev, D. M. Wojchowski, P. Toran, C. R. Worsfold, M. P. Castaldi, J. C. Silva, Affinity-bead assisted mass spectrometry (Affi-BAMS): A multiplexed microarray platform for targeted proteomics. *Int. J. Mol. Sci.* **21**, 2016 (2020).
38. A. B. Chambliss, P. H. Wu, W. C. Chen, S. X. Sun, D. Wirtz, Simultaneously defining cell phenotypes, cell cycle, and chromatin modifications at single-cell resolution. *FASEB J.* **27**, 2667–2676 (2013).
39. A. Peserico, C. Simone, Physical and functional HAT/HDAC interplay regulates protein acetylation balance. *J. Biomed. Biotechnol.* **2011**, 1–10 (2011).

40. R. Fischer, A. Konkel, H. Mehling, K. Blossey, A. Gapelyuk, N. Wessel, C. von Schacky, R. Dechend, D. N. Muller, M. Rothe, F. C. Luft, K. Weylandt, W. H. Schunck, Dietary omega-3 fatty acids modulate the eicosanoid profile in man primarily via the CYP-epoxygenase pathway. *J. Lipid Res.* **55**, 1150–1164 (2014).
41. E. Fabbri, T. Tanaka, Y. An, M. Zoli, S. Bandinelli, J. M. Guralnik, E. M. Simonsick, C. M. Boyd, S. A. Studenski, T. B. Harris, L. Ferrucci, Loss of weight in obese older adults: A biomarker of impending expansion of multimorbidity? *J. Am. Geriatr. Soc.* **63**, 1791–1797 (2015).
42. B. Fougere, J. E. Morley, Editorial: Weight loss is a major cause of frailty. *J. Nutr. Health Aging* **21**, 933–935 (2017).
43. O. Chatzidoukaki, E. Goulielmaki, B. Schumacher, G. A. Garinis, DNA damage response and metabolic reprogramming in health and disease. *Trends Genet.* **36**, 777–791 (2020).
44. D. Edifizi, H. Nolte, V. Babu, L. Castells-Roca, M. M. Mueller, S. Brodesser, M. Krüger, B. Schumacher, Multilayered reprogramming in response to persistent DNA damage in C. elegans. *Cell Rep.* **20**, 2026–2043 (2017).
45. C. Milanese, C. R. Bombardieri, S. Sepe, S. Barnhoorn, C. Payán-Goméz, D. Caruso, M. Audano, S. Pedretti, W. P. Vermeij, R. M. C. Brandt, A. Gyenis, M. M. Wamelink, A. S. de Wit, R. C. Janssens, R. Leen, A. B. P. van Kuilenburg, N. Mitro, J. H. J. Hoeijmakers, P. G. Mastroberardino, DNA damage and transcription stress cause ATP-mediated redesign of metabolism and potentiation of anti-oxidant buffering. *Nat. Commun.* **10**, 4887 (2019).
46. J. Xiong, H. Kawagishi, Y. Yan, J. Liu, Q. S. Wells, L. R. Edmunds, M. M. Fergusson, Z.-X. Yu, I. I. Rovira, E. L. Brittain, M. J. Wolfgang, M. J. Jurczak, J. P. Fessel, T. Finkel, A metabolic basis for endothelial-to-mesenchymal transition. *Mol. Cell* **69**, 689–698.e7 (2018).
47. S. Schoors, U. Bruning, R. Missiaen, K. C. S. Queiroz, G. Borgers, I. Elia, A. Zecchin, A. R. Cantelmo, S. Christen, J. Goveia, W. Heggermont, L. Goddé, S. Vinckier, P. P. van Veldhoven, G. Eelen, L. Schoonjans, H. Gerhardt, M. Dewerchin, M. Baes, K. de Bock, B. Ghesquière, S. Y. Lunt, S. M. Fendt, P. Carmeliet, Fatty acid carbon is essential for dNTP synthesis in endothelial cells. *Nature* **520**, 192–197 (2015).
48. W. Dang, K. K. Steffen, R. Perry, J. A. Dorsey, F. B. Johnson, A. Shilatifard, M. Kaeberlein, B. K. Kennedy, S. L. Berger, Histone H4 lysine 16 acetylation regulates cellular lifespan. *Nature* **459**, 802–807 (2009).
49. W. Giblin, M. E. Skinner, D. B. Lombard, Sirtuins: Guardians of mammalian healthspan. *Trends Genet.* **30**, 271–286 (2014).
50. V. Gonzalez-Covarrubias, M. Beekman, H. W. Uh, A. Dane, J. Troost, I. Paliukhovich, F. M. Kloet, J. Houwing-Duistermaat, R. J. Vreeken, T. Hankemeier, E. P. Slagboom, Lipidomics of familial longevity. *Aging Cell* **12**, 426–434 (2013).
51. S. Sugawara, T. Honma, J. Ito, R. Kijima, T. Tsuduki, Fish oil changes the lifespan of Caenorhabditis elegans via lipid peroxidation. *J. Clin. Biochem. Nutr.* **52**, 139–145 (2013).
52. W. Qi, G. E. Gutierrez, X. Gao, H. Dixon, J. A. McDonough, A. M. Marini, A. L. Fisher, The ω-3 fatty acid α-linolenic acid extendsCaenorhabditis eleganslifespan via NHR-49/PPARα and oxidation to oxylipins. *Aging Cell* **16**, 1125–1135 (2017).
53. M. A. Perez, L. Magtanong, S. J. Dixon, J. L. Watts, Dietary lipids induce ferroptosis in Caenorhabditiselegans and human cancer cells. *Dev. Cell* **54**, 447–454.e4 (2020).
54. C. N. Serhan, S. Yacoubian, R. Yang, Anti-inflammatory and proresolving lipid mediators. *Annu. Rev. Pathol.* **3**, 279–312 (2008).
55. J. Zhao, L. Zhang, X. Mu, C. Doebelin, W. Nguyen, C. Wallace, D. P. Reay, S. J. McGowan, L. Corbo, P. R. Clemens, G. M. Wilson, S. C. Watkins, L. A. Solt, M. D. Cameron, J. Huard, L. J. Niedernhofer, T. M. Kamenecka, P. D. Robbins, Development of novel NEMO-binding domain mimetics for inhibiting IKK/NF-κB activation. *PLoS Biol.* **16**, e2004663 (2018).
56. T. Lu, Y. Pan, S. Y. Kao, C. Li, I. Kohane, J. Chan, B. A. Yankner, Gene regulation and DNA damage in the ageing human brain. *Nature* **429**, 883–891 (2004).
57. C. R. Keenan, R. S. Allan, Epigenomic drivers of immune dysfunction in aging. *Aging Cell* **18**, e12878 (2019).
58. K. C. Reddy, T. Dror, J. N. Sowa, J. Panek, K. Chen, E. S. Lim, D. Wang, E. R. Troemel, An intracellular pathogen response pathway promotes proteostasis in C. elegans. *Curr. Biol.* **27**, 3544–3553.e5 (2017).
59. E. Leyva-Díaz, N. Stefanakis, I. Carrera, L. Glenwinkel, G. Wang, M. Driscoll, O. Hobert, Silencing of repetitive DNA Is controlled by a member of an unusual Caenorhabditis elegans gene family. *Genetics* **207**, 529–545 (2017).
60. J. T. Bulcha, G. E. Giese, M. Z. Ali, Y.-U. Lee, M. D. Walker, A. D. Holdorf, L. S. Yilmaz, R. C. Brewster, A. J. M. Walhout, A persistence detector for metabolic network rewiring in an animal. *Cell Rep.* **26**, 460–468.e4 (2019).
61. C. McQuin, A. Goodman, V. Chernyshev, L. Kamentsky, B. A. Cimini, K. W. Karhohs, M. Doan, L. Ding, S. M. Rafelski, D. Thirstrup, W. Wiegraebe, S. Singh, T. Becker, J. C. Caicedo, A. E. Carpenter, CellProfiler 3.0: Next-generation image processing for biology. *PLoS Biol.* **16**, e2005970 (2018).
62. A. Sandhu, V. Singh, Total triglyceride quantification in Caenorhabditis elegans. *Bio-protocol* **10**, e3819 (2020).
63. P. S. Chen, T. Y. Toribara, H. Warner, Microdetermination of phosphorus. *Anal. Chem.* **28**, 1756–1758 (1956).
64. D. Zhu, X. Wu, J. Zhou, X. Li, X. Huang, J. Li, J. Wu, Q. Bian, Y. Wang, Y. Tian, NuRD mediates mitochondrial stress-induced longevity via chromatin remodeling in response to acetyl-CoA level. *Sci. Adv.* **6**, eabb2529 (2020).
65. A. C. Lau, K. P. Zhu, E. A. Brouhard, M. B. Davis, G. Csankovszki, An H4K16 histone acetyltransferase mediates decondensation of the X chromosome in C. elegans males. *Epigenetics Chromatin* **9**, 44 (2016).
66. Y. Liao, G. K. Smyth, W. Shi, featureCounts: An efficient general purpose program for assigning sequence reads to genomic features. *Bioinformatics* **30**, 923–930 (2014).
67. C. Trapnell, B. A. Williams, G. Pertea, A. Mortazavi, G. Kwan, M. J. van Baren, S. L. Salzberg, B. J. Wold, L. Pachter, Transcript assembly and quantification by RNA-seq reveals unannotated transcripts and isoform switching during cell differentiation. *Nat. Biotechnol.* **28**, 511–515 (2010).
68. A. J. Frey, D. R. Feldman, S. Trefely, A. J. Worth, S. S. Basu, N. W. Snyder, LC-quadrupole/Orbitrap high-resolution mass spectrometry enables stable isotope-resolved simultaneous quantification and 13C-isotopic labeling of acyl-coenzyme A thioesters. *Anal. Bioanal. Chem.* **408**, 3651–3658 (2016).
69. N. W. Snyder, G. Tombline, A. J. Worth, R. C. Parry, J. A. Silvers, K. P. Gillespie, S. S. Basu, J. Millen, D. S. Goldfarb, I. A. Blair, Production of stable isotope-labeled acyl-coenzyme A thioesters by yeast stable isotope labeling by essential nutrients in cell culture. *Anal. Biochem.* **474**, 59–65 (2015).
70. S. E. Wenzel, Y. Y. Tyurina, J. Zhao, C. M. S.t. Croix, H. H. Dar, G. Mao, V. A. Tyurin, T. S. Anthonymuthu, A. A. Kapralov, A. A. Amoscato, K. Mikulska-Ruminska, I. H. Shrivastava, E. M. Kenny, Q. Yang, J. C. Rosenbaum, L. J. Sparvero, D. R. Emlet, X. Wen, Y. Minami, F. Qu, S. C. Watkins, T. R. Holman, A. P. Van Demark, J. A. Kellum, I. Bahar, H. Bayır, V. E. Kagan, PEBP1 wardens ferroptosis by enabling lipoxygenase generation of lipid death signals. *Cell* **171**, 628–641.e26 (2017).

Acknowledgments: We thank J. Yanowitz, A. Ghazi, T. Lamintina, and M. Gill for RNAi and for insightful scientific discussions; C. Worsfold and J. C. Silva for technical assistance with BAMS analysis; and T. Finkel for comments on the manuscript. **Funding:** This work was funded by NIH grants R00AG049126 (A.U.G.), R01GM132261 (N.W.S.), NIH ZIA AG000679 (P.S.), AI145406, CA165065, CA243142, AI068021, GM113908, HL114453, AI156924, NS076511, AI156923, and NS061817 (H.B. and V.K.). Metabolomics assistance was provided by the Metabolomic Core at Pitt S10OD023402. Strains were provided by the Caenorhabditis Genetics Center, which is funded by the NIH Office of Research Infrastructure Programs (P40 OD010440). **Author contributions:** A.U.G. and S.Ham. provided study design. S.Ham. and A.U.G. performed most of the experiments. S. Han, H.S., E.S., and A.S. provided technical assistance and blinded ORO imaging. S.Ham., and T.A., performed metabolomics and analysis. S.Ham., T.A., H.B., and V.K. performed lipidomics and analysis. H.L.P. and N.W.S. performed acetyl-CoA measurements. T.A. performed BAMS analysis. P.S. helped with intellectual and technical expertise on epigenetic analysis. S.Ham. and A.U.G. drafted the manuscript with the help of all co-authors. A.U.G. supervised the study. **Competing interests:** T.A. is an employee of Adeptrix corporation. All other authors declare that they have no competing interests. **Data and materials availability:** All data needed to evaluate the conclusions in the paper are present in the paper and/or the Supplementary Materials. The -omic data have been deposited and are available as indicated in Materials and Methods.

Submitted 26 July 2021
Accepted 23 December 2021
Published 16 February 2022
10.1126/sciadv.abl6083